Composite Structures 392 (2026) 120551

Contents lists available at ScienceDirect

Composite Structures

journal homepage: www.elsevier.com/locate/compstruct

Analysis of the tensile effects of platelet architectures for woven engineered pre-impregnated platelets

Alessandro Masetti Placci [a,c,*], Luca Bernini [a,b], Paolo Albertelli [a,b]

[a] Politecnico di Milano, Department of Mechanical Engineering, via La Masa, 1, Milan, 20156, Lombardy, Italy
[b] MUSP Macchine Utensili Sistemi di Produzione, strada della Torre della Razza, Piacenza, 29122, Emilia-Romagna, Italy
[c] Racing Bulls S.p.A, Via Boaria 229, Faenza, 48018, Emilia-Romagna, Italy

ARTICLE INFO

Keywords:
Prepreg platelets
Carbon fibre
Discontinuous composites
Woven CFRP

ABSTRACT

Manufacturing scrap from virgin pre-impregnated (prepreg) carbon fibre remains a major composite waste stream, motivating research to characterise this high-value material for structural applications. This work characterises the tensile response of woven engineered prepreg platelet (EPP) laminates and quantifies the influence of key architectural parameters in a design of experiments: platelet length and width, length and width superposition, and ply count (l_p, w_p, δl, δw, n_p, respectively). Tensile properties and fracture morphologies were measured for each architecture set, while factor effects were evaluated using *analysis of variance (ANOVA)* with linear and normalised response models alongside shear-lag and fracture-mechanics interpretation. Predictive and interpretative models were produced for all tensile values, including ultimate tensile strength, Young's modulus, and strain at failure, which showed that platelet dimensions and superpositions jointly govern load transfer, with selective arrangements retaining up to 90% of baseline stiffness while limiting strength penalties. Normalisation improved interpretability by reducing thickness masking and fracture analysis identified matrix-rich inter-ply regions as preferential initiation sites with propagation trends linked to superposition balance. Overall, the findings establish woven EPPs as tuneable discontinuous composites with measurable architecture–property relationships and provide a validated basis for future optimisation and damage-aware modelling.

1. Introduction

The introduction of carbon fibre reinforced polymer (CFRP) composites has revolutionised various industries, including aerospace, automotive, sporting goods, renewable energy, and other high-performance sectors is driven by their favourable combination of low density, high specific strength and stiffness [1–4]. However, growing demand and extensive use of CFRP materials has led to a rapid growth of composite waste streams, encompassing both manufacturing waste and end-of-life products [3]. In parallel, thermoset systems continue to dominate composite supply chains, accounting for 72% of the global market demand in 2025 [5]. This creates a pressing need for circular pathways that retain the value embedded in high-grade reinforcement materials [6].

Pre-impregnated (prepreg) thermoset CFRP is particularly affected by waste generation, as approximately 40% of all virgin prepreg material is wasted as offcuts or scrap, and additional waste also arises from expired material [7,8]. Thermoset prepreg waste can be classified as uncrosslinked or crosslinked waste [9]. Crosslinked waste (post-cure scrap or end-of-life components) is generally referred to as *recycling*, which focuses on reclaiming fibres via pyrolysis [10], chemical solvolysis [11], or mechanical processing [12]. Meanwhile, uncrosslinked waste (manufacturing trimmings or expired rolls) enables *repurposing* or *remanufacturing*, where the objective is to preserve and reconfigured the feedstock into new high-value composite forms [6,9].

Within this context, long discontinuous CFRP occupies an intermediate design space between conventional continuous fibre laminates and short-fibre (SF) moulding compounds. A common umbrella term is discontinuous carbon fibre composites (DCFC), which encompasses CFRP systems where the primary lamination is not continuous [13]. Several DCFC material forms have been explored, including prepreg platelet moulded composites (PPMCs) [14–16] and tow-based discontinuous composites (TBDCs) [17,18]. This work focuses on platelet-based reinforcements, also referred to as flakes, chips, patches, strands, or tows [14,15,17,19,20], which represent the largest discontinuous elements within DCFCs and enable direct control of reinforcement length, overlap, spatial arrangement, and orientation. Crucially, beyond constituent selection, DCFCs may be more generically grouped

* Corresponding author at: Politecnico di Milano, Department of Mechanical Engineering, via La Masa, 1, Milan, 20156, Lombardy, Italy.
E-mail addresses: alessandro.masetti@polimi.it (A.M. Placci), luca1.bernini@polimi.it (L. Bernini), paolo.albertelli@polimi.it (P. Albertelli).

https://doi.org/10.1016/j.compstruct.2026.120551
Received 5 March 2026; Received in revised form 16 May 2026; Accepted 11 June 2026
Available online 22 June 2026

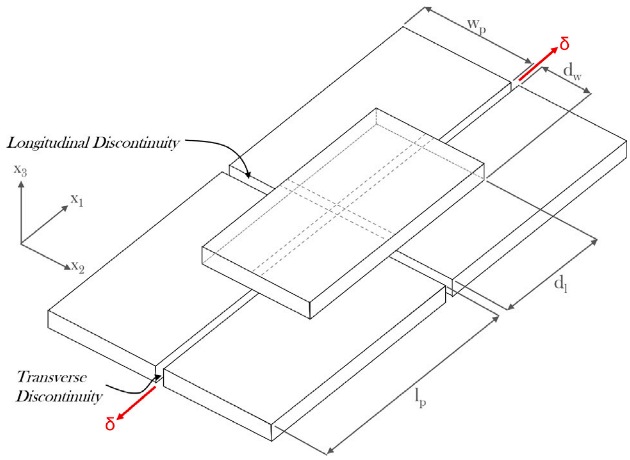

Fig. 1. Schematic demonstrating the woven engineered prepreg platelet design of experiments.

into *irregular* and *regular* morphologies. Irregular morphologies have a stochastic deposition of discontinuous reinforcement, typically introducing pronounced local heterogeneity and reducing effective properties relative to the feed material; regular morphologies employ designed and repeatable patterns with controllable stacking sequences [15] (Fig. 1).

Platelet-based systems have therefore attracted significant research attention, combining experimental characterisation with analytical and numerical modelling methodologies to understand stress transfer, damage mechanisms, and morphology-driven performance [21–23]. Nakagawa et al. [24] investigated the flexural behaviour of DCFC panels produced from repurposed aerospace prepreg, reporting increasing flexural modulus and strength with platelet length, while increasing thickness produced negligible benefits, but reduced scatter. Kravchenko et al. [14,25] examined both regular and irregular morphology PPMCs in uniaxial tension, while Pipes et al. [15,16] further quantified the role of critical platelet length in determining dominant failure modes, and analysed notch sensitivity for PPMC specimens. Collectively, these studies indicate that the global response of platelet-based composites is governed by morphology-dependent three-dimensional stress transfer and the competition between platelet rupture and inter-platelet separation.

More broadly, platelet composites exemplify hierarchical material behaviour, where the meso-scale architecture can dominate emergent mechanical properties [26]. Performance is therefore not dictated solely by constituent properties, but by platelet dimensions, overlap, arrangement, and the repeatability of the meso-architecture. The present work centres on architected platelet feedstock with a controlled regular morphology; the resulting composite system is herein referred to as an *engineered prepreg platelet* (EPP) system. The term *EPP* is adopted to emphasise the engineered nature of the platelet architecture while distinguishing it from the broader DCFC classification and from process-specific terminology such as PPMCs or the 2D morphologies of Brick-and-Mortar (BaM) structures.

While much of the existing experimental and modelling research has focused on unidirectional (UD) prepreg platelet systems, woven CFRP prepregs remain widely used in high-performance sectors due to manufacturing advantages including improved formability for complex geometries, more balanced in-plane properties, and simplified lay-up relative to UD laminates [27,28]. Motivated by this gap, this paper presents an experimental investigation of *woven* EPP composite systems. Since the structural response of EPPs is governed by platelet *architecture* (comprising platelet dimensions, overlap, spatial arrangement, and stacking sequence), the aim of this work is to quantify how these design variables control the tensile stiffness, strength, and strain at failure. Tensile behaviour is considered as a primary screening modality for material viability and as a practical basis for subsequent design decisions and architecture optimisation [29,30].

Accordingly, this work investigates and characterises the elastic tensile and failure response of woven EPP laminate architectures while controlling variations in key platelet parameters, with the aim of establishing structure–property relationships for architected discontinuous prepreg systems. Analysis of variance (*ANOVA*) is implemented using linear regression modelling with the goals of producing an interpretative model that can accurately quantify the contribution of each architectural factor being investigated, effectively capturing and predicting the observed variability in the experimental dataset, and a predictive model that could be used to assess new EPP architectures and arrangements.

The work is structured as follows. Section 2 describes the manufacturing procedure, conception of the design of experiments, fracture analysis undertaken post tensile testing and the analysis of variance implemented. Meanwhile Section 3 details the tensile properties for the tested EPP architectures, divided into 4-ply (Section 3.1), 6-ply (Section 3.2), and 8-ply (Section 3.3) arrangement results. The analysis of variance and various models are discussed in Section 4, and 5 summarises the key findings.

2. Materials and methods

This work investigates how controlled variations in platelet architecture affect the elastic tensile and failure behaviours of woven EPP laminates. This section follows the workflow summarised in the graphical abstract (Fig. 2), with the intention of producing a predictive and interpretative model to analyse and characterise EPP performance. A Design of Experiments (DoE) was defined to define all relevant parameters, highlighted in Section 2.1, with the manufacturing methodology for the tensile testing of the specimens in Section 2.2, and the subsequent extraction of tensile properties for each arrangement is outlined in Section 2.3 which includes the Young's modulus (E), ultimate tensile strength (*UTS*), and strain at failure (ε_f). This was followed by a fracture analysis (Section 2.4) which characterised the dominant failure modes for all specimens, and was utilised in the *Analysis of Variance (ANOVA)* and linear regression modelling to quantify the main effects and interactions (Section 2.5).

2.1. Design of experiments

The DoE and associated experimental campaign were developed from the broader understanding established in previous studies on platelet-based prepreg composites, particularly the role of platelet dimensions and overlap in governing tensile response and dominant failure modes [14,31]. Building on this foundation, the present study extends the parameter space to woven EPP architectures by systematically varying the key geometric and superposition variables considered most relevant to load transfer and damage development.

The DoE was conceived according to a full factorial design in order to test the effect of different platelet architectures on the mechanical performances of the final material. The full factorial design consisted of a $n_r \cdot (2^k + 1)$ design, where n_r is the number of replicas, k is the number of factors considered, each assuming two-levels. The central point was introduced to check for the presence of model curvature. In our case, five different parameters were chosen. The parameters were defined in a way that allows modular configuration of the platelets. The tensile testing therefore ensured the computation of performances of a Representative Volume Element (RVE) of the final composite material. Furthermore, n_r was set to 4, in order to have enough statistical information on the effect of platelet arrangements on the material properties. That said, the DoE ended up in a total of 33 platelet arrangements, leading to 132 manufactured EPP tensile specimens, incorporating variations and key geometric parameters. The five key parameters of the DoE are reported in the following, and is illustrated in Fig. 1:

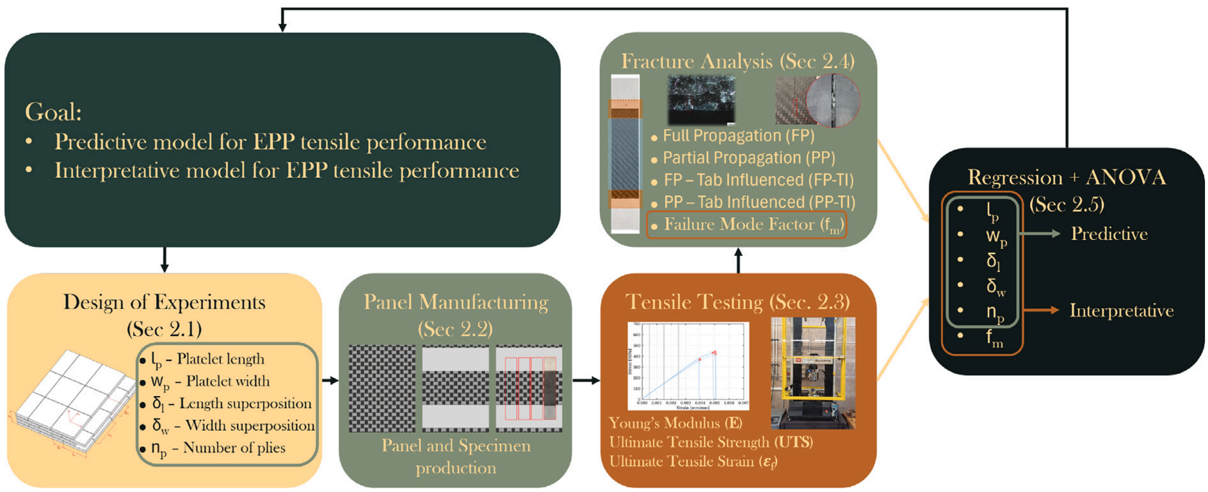

Fig. 2. Graphical overview of the experimental methodology and analysis workflow.

- n_l, the number of platelets within the nominal specimen length (l_0, noted as gauge length). This parameter is defined as $\frac{l_0}{l_p}$, where l_p is the platelet length. n_l was chosen to be 4 and 6 at the extremes of the DoE, and 5 at the central point.
- n_w, the number of platelets within the nominal specimen width (w_0). This parameter is defined as $\frac{w_0}{w_p}$, where w_p is the platelet width. n_w was chosen to be 1 and 3 at the extremes of the DoE, and 2 at the central point.
- δl, the platelet superposition ratio, in the length direction, often referred to as overlap ratio. This parameter is defined as $\frac{l_p}{d_l}$, where d_l is the platelet superposition in length. δl was chosen to be 2 and 4 at the extremes of the DoE, 3 at the central point.
- δw, the platelet superposition ratio, in the width direction, often referred to as overlap ratio. This parameter is defined as $\frac{w_p}{d_w}$, where d_w is the platelet superposition in width. δw was chosen to be 2 and 4 at the extremes of the DoE, 3 at the central point.
- n_p, the number of plies (layers) adopted for the EPP architecture. n_p assumed the values 4 and 8 at the extremes of the DoE, and consequently 6 at the central point.

The full experimental design is detailed in Table 1. For clarity, the term *EPP architecture* refers to a unique combination of platelet DoE parameters (l_p, w_p, δl, δw) and is defined independently of ply count. A specific realisation of a given EPP architecture at a particular ply number n_p is herein termed a *platelet arrangement*.

To enable direct comparison, continuous woven specimens were also produced for all ply numbers ($n_p = 4, 6, 8$) with the same number of replicas n_r.

2.2. Panel manufacturing

All specimens were produced by Blacks Composites [32] at their facility in Faenza, Italy. Precursor woven prepreg plies were initially cut from a prepreg roll into rectangular sheets measuring 300×265 mm, conforming to the final panel's dimensions.

The material used in this work is a CFRP prepreg consisting of $M46J$ carbon fibre reinforcements and a $ER450$ thermoset epoxy resin, with an areal weight of $200\,\mathrm{g/m^2}$ produced by Composite Materials Italy (CIT) [33]. This 2 × 2 twill high modulus fabric has a cured ply thickness of 0.22 mm, a fibre volume fraction of 60 wt%, and was supplied by Racing Bulls S.p.A [30]. Its mechanical properties are given in Table 2.

To achieve precise and repeatable platelet geometries while streamlining the manufacturing flow, the Lectra IQ50 automated ply cutter (plotter) was employed [34]. The plotter cut and scored the platelet discontinuities on the prepreg fabric roll, along the platelet length and width respectively, preserving the ply's homogeneity for easier handling while maintaining control and consistency between plies to minimise manufacturing errors before cutting the rectangular sheets.

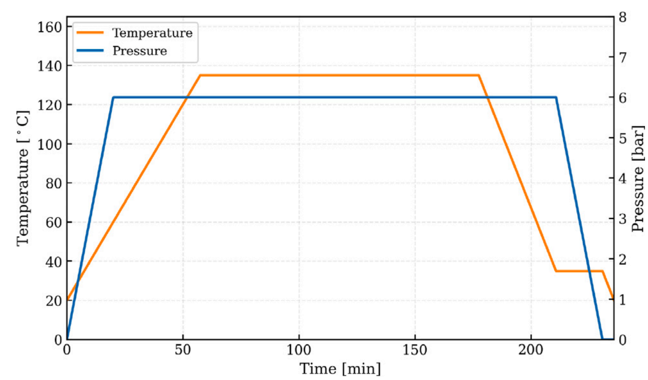

Fig. 3. Graph illustrating the pressure and temperatures of the cure cycle for the production of specimens.

During the lay-up procedure, the scored transverse discontinuities were incised manually by the laminator prior to being laminated following a predefined stacking sequence on a flat carbon/epoxy mould. Aluminium positioning loose tools, corresponding to the final panel dimensions, were used to align the prepreg sheets and maintain the nominal panel geometry during curing. After stacking, an aluminium counter-mould was placed over the laminate to promote uniform compaction and covered with a non-perforated release film and breather cloth, prior to being enveloped in a vacuum bag, and vacuum-sealed in preparation for curing [30].

The panel was subsequently placed in an autoclave with the following cure cycle. Initially, the temperature was ramped up to 135 °C at a rate of 2 °C/min, while the pressure increased to 6 bar at a rate of 0.3 bar/min. This temperature and pressure were maintained for 120 min, after which the panels were allowed to cool under pressure to 35 °C at a rate of 3 °C/min. Then the pressure was released at a rate of 0.3 bar/min. The cycle is represented in Fig. 3.

Once cured, the panel was removed from the mould (Fig. 4a). Glass fibre and epoxy end-tabs were bonded using an autoclave-curable adhesive, ensuring a central 138 mm gauge length (Fig. 4b). Following the adhesive's cure cycle, the panel was cut into four tensile specimens using a water jet (Fig. 4c).

Table 1
Design of experiments. *Order* is the manufacturing and testing order; n_l is the platelet number per nominal specimen length; n_w is the platelet number per nominal specimen width; δl is the length platelet superposition ratio; δw is the width platelet superposition ratio; n_p is the number of plies. Additional parameters are reported for the sake of clarity: l_p is the platelet length; w_p is the platelet width; d_l is the length superposition; d_w is the width superposition.

ID	Order	n_l	n_w	δl	δw	n_p	l_p	w_p	d_l	d_w
–	–	[#]	[#]	[#] ([%])	[#] ([%])	[#]	[mm]	[mm]	[mm]	[mm]
0	113–116	4	1	2 (50%)	2 (50%)	4	34.5	45.0	17.3	22.5
1	53–56	4	1	2 (50%)	2 (50%)	8	34.5	45.0	17.3	22.5
2	105–108	4	1	2 (50%)	4 (25%)	4	34.5	45.0	17.3	11.3
3	81–84	4	1	2 (50%)	4 (25%)	8	34.5	45.0	17.3	11.3
4	61–64	4	1	4 (25%)	2 (50%)	4	34.5	45.0	8.6	22.5
5	13–16	4	1	4 (25%)	2 (50%)	8	34.5	45.0	8.6	22.5
6	9–12	4	1	4 (25%)	4 (25%)	4	34.5	45.0	8.6	11.3
7	41–44	4	1	4 (25%)	4 (25%)	8	34.5	45.0	8.6	11.3
8	29–32	4	3	2 (50%)	2 (50%)	4	34.5	15.0	17.3	7.5
9	77–80	4	3	2 (50%)	2 (50%)	8	34.5	15.0	17.3	7.5
10	69–72	4	3	2 (50%)	4 (25%)	4	34.5	15.0	17.3	3.8
11	109–112	4	3	2 (50%)	4 (25%)	8	34.5	15.0	17.3	3.8
12	121–124	4	3	4 (25%)	2 (50%)	4	34.5	15.0	8.6	7.5
13	117–120	4	3	4 (25%)	2 (50%)	8	34.5	15.0	8.6	7.5
14	101–104	4	3	4 (25%)	4 (25%)	4	34.5	15.0	8.6	3.8
15	65–68	4	3	4 (25%)	4 (25%)	8	34.5	15.0	8.6	3.8
16	97–100	6	1	2 (50%)	2 (50%)	4	23.0	45.0	11.5	22.5
17	17–20	6	1	2 (50%)	2 (50%)	8	23.0	45.0	11.5	22.5
18	37–40	6	1	2 (50%)	4 (25%)	4	23.0	45.0	11.5	11.3
19	93–96	6	1	2 (50%)	4 (25%)	8	23.0	45.0	11.5	11.3
20	73–76	6	1	4 (25%)	2 (50%)	4	23.0	45.0	5.8	22.5
21	25–28	6	1	4 (25%)	2 (50%)	8	23.0	45.0	5.8	22.5
22	89–92	6	1	4 (25%)	4 (25%)	4	23.0	45.0	5.8	11.3
23	5–8	6	1	4 (25%)	4 (25%)	8	23.0	45.0	5.8	11.3
24	49–52	6	3	2 (50%)	2 (50%)	4	23.0	15.0	11.5	7.5
25	21–24	6	3	2 (50%)	2 (50%)	8	23.0	15.0	11.5	7.5
26	129–132	6	3	2 (50%)	4 (25%)	4	23.0	15.0	11.5	3.8
27	125–128	6	3	2 (50%)	4 (25%)	8	23.0	15.0	11.5	3.8
28	57–60	6	3	4 (25%)	2 (50%)	4	23.0	15.0	5.8	7.5
29	45–48	6	3	4 (25%)	2 (50%)	8	23.0	15.0	5.8	7.5
30	85–88	6	3	4 (25%)	4 (25%)	4	23.0	15.0	5.8	3.8
31	33–36	6	3	4 (25%)	4 (25%)	8	23.0	15.0	5.8	3.8
32	1–4	5	2	3 (33%)	3 (33%)	6	27.6	22.5	9.2	7.5

Table 2
Material properties for $M46J/ER450$ carbon fibre epoxy resin Woven CFRP [33].

Material properties	$M46J/ER450$
Young's modulus, E [GPa]	109.8
Ultimate tensile strength, UTS [MPa]	674.1
Strain to failure, ε_f [%]	0.63
Shear modulus, G_{12} [GPa]	3.70
Poisson's ratio, υ_{12}	0.04

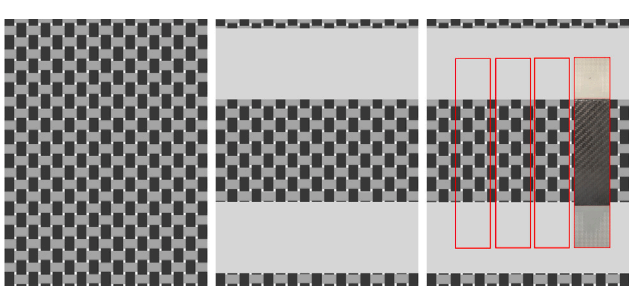

(a) (b) (c)

Fig. 4. Manufacturing process of the Woven EPP specimens (a) Characteristic EPP panel (b) Schematic detailing the bonded end-tabs (c) Outline of specimen locations and manufactured specimen example.

2.3. Tensile testing

The tensile specimens were tested according to the ASTM D 3039 standard [35] for polymer matrix composites, with a modified specimen width to accommodate manufacturing constraints related to specimen platelet production, and minimum incisions lengths for the plotter as advised by Racing Bulls S.p.A. The experimental campaign utilised specimens measuring 250 × 45 mm with 56 mm long end-tabs on either end of the specimen for the universal testing machine's (UTM) grips. The resulting nominal specimen length and width, (l_0 and w_0), are 138 mm and 45 mm, respectively. These nominal specimen dimensions, alongside the previously outlined DoE factors, the corresponding platelet parameters are:

- l_p, platelet lengths of 34.5, 27.6, and 23.0 mm.
- w_p, platelet widths of 45.0, 15.0, and 22.5 mm.
- δl, platelet length superposition of 50%, 25%, and 33% of the platelet length.
- δw, platelet width superposition of 50%, 25%, and 33% of the platelet width.

Each EPP architecture was tested using an MTS Alliance RT 100 UTM with a 80 kN load cell at a quasi-static speed of 2 mm/min. The specimens were tested using wedge-action grips acting on the bonded end-tabs, with an initial grip separation of 130 mm for all specimens. The loading was stopped after the complete fracture of the specimen occurred. Force ($F(t)$) was recorded from the UTM load cell and a clip-on axial extensometer was used to measure the extension of the specimens under tension, with a gauge length of 50 mm, positioned approximately at mid-gauge. The extensometer remained attached throughout the test,

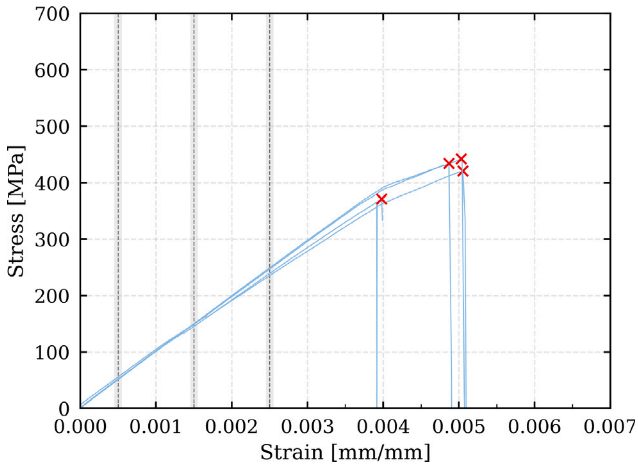

Fig. 5. EPP #30 stress–strain curves demonstrating the data extrapolation, including the target strains locations (ε_i^*) alongside the *UTS* and ε_f and ε_f measurement locations from the red cross.

and was not removed prior to specimen failure, such that the ε_f was obtained directly from the extensometer measurement.

Engineering stress was computed as:

$$\sigma(t) = \frac{F(t)}{A_0} \quad (1)$$

where A_0 is the initial cross-sectional area of the specimen. Specimen width and thicknesses were measured using vernier calipers at three equally spaced locations within the specimen's gauge length l_0 prior to testing. The mean width and thickness values were used to define A_0 for each specimen.

The UTS was taken as the maximum engineering stress:

$$UTS = \max\left[\sigma(t)\right] \quad (2)$$

While the strain at failure was defined as the measured extensometer strain at the time corresponding to σ_{UTS};

$$\varepsilon_f = \varepsilon(t)\Big|_{t=t_f} \quad (3)$$

The E was extracted from the initial linear-elastic response using a simple secant-based approach at prescribed strain levels. Three target strains were defined to avoid initial loading artefacts while remaining below any observed stiffness changes (Fig. 5): $\varepsilon^* = \{0.0005, 0.0015, 0.0025\}$. For each target strain ε_i^*, the recorded data point with strain closest to ε_i^* was selected, and the corresponding stress–strain pair $(\varepsilon_i, \sigma_i)$ was used to compute the Young's modulus.

$$E_i = \frac{\sigma_i}{\varepsilon_i} \quad (4)$$

The reported specimen's E was taken as the mean of the three target values;

$$E = \frac{E_{0.0005} + E_{0.0015} + E_{0.0025}}{3} \quad (5)$$

2.4. Fracture analysis

Following tensile testing, all specimens were examined to identify the dominant fracture mechanisms, the apparent crack initiation region, and the extent of crack propagation. The fracture analysis combined visual inspection, macroscopic observations, microscopic analyses, and Scanning Electron Microscopy (SEM) of selected fracture surfaces. Macroscopic inspections were utilised to classify the global failure mode and whether the failure occurred within the nominal gauge region or within the tab-proximate region, Fig. 6. Optical microscopy was used to examine local delamination, fibre pull-out, and matrix-rich discontinuous regions. SEM observations were conducted on selected specimens to identify local fracture features associated with their failure classification, including fibre pull-out, tow and fibre fracture, matrix cracks, and interfacial separation at platelet-to-platelet surfaces.

The fracture analysis was interpreted using the stress-transfer framework commonly adopted for discontinuous platelet composites. Under uniaxial tensile loading, the axial stress carried by a platelet is not transferred directly through the platelet ends, and instead through interfacial shear stresses acting over the overlap region between neighbouring platelets. Consequently, the axial platelet stress within a platelet develops over a finite transfer length governed by the platelet length and longitudinal overlap, while interlaminar shear stresses remain concentrated near platelet edges and overlap boundaries [36,37]. For a woven EPP laminate, the stress-transfer process is three-dimensional with the primary axial load path being governed by σ_{11} and interlaminar shear σ_{13}, while the transverse fibres activate σ_{22} and σ_{23}. Local through-thickness peel stress, σ_{33}, may also develop at platelet edges, overlap transitions, and matrix rich inter-ply zones. However, σ_{33} is not expected to contribute uniformly through the laminate thickness. At internal platelet interfaces, these local peel stresses are balanced and constrained by neighbouring plies, whereas at the outer plies and free surfaces, this balancing is non-existent. As a result, peel-driven interlaminar shear effects are expected to be more consequential in the thinner 4-ply arrangements, where the free surfaces represent a larger fraction of the laminate. The combined action of σ_{11}, σ_{22}, σ_{13}, σ_{23}, and σ_{33} contributes to controlling the competition between platelet fracture, interfacial delamination, and mixed fracture paths, illustrated in Fig. 7.

The role of platelet geometry throughout this work was interpreted through three complementary descriptors. The first is the platelet length-to-thickness ratio, $\alpha = l_p/t_p$, which governs the platelet's ability to develop sufficient axial stress through shear-lag transfer. A larger α increases the overlap length and discerns whether the platelet can develop stresses approaching the composite's tensile strength, promoting platelet rupture, or if interfacial shear remains dominant and failure is initiated through interfacial failure. This parameter is consistent with Platelet Critical Length (L_C) descriptions, where the transition between interfacial failure and platelet rupture is governed by the overlap length, interfacial shear strength, platelet tensile strength, and α [14,16]. The second descriptor is the platelet width-to-thickness ratio $\omega = w_p/t_p$, which for a uniaxial tensile test must be implemented differently as the relevance of W_c and ω is weakened as the far-field strain remains dominated by the principal loading axis. As a result, these parameters influence the local stability of damage progression with the secondary fibre reinforcement direction. The final descriptor is the available bonded area, governed by l_p, w_p, δl, and δw, which determines the area over which stress-transfer can occur. Reduced overlap areas results in the local shear and peel stresses acting through platelet edges to become more concentrated, increasing the likelihood of interfacial failure and unstable delamination.

The dominant failure modes where therefore classified according to the final crack morphology, while recognising that the final fracture surface may result from several interacting damage mechanisms. These failure modes were defined as:

- **Partial propagation (PP):** where the crack propagates through the laminate thickness or along a dominant delamination path, but the specimen retains partial global continuity after peak load (Fig. 8a);
- **Full propagation (FP):** where the crack propagates through the entire laminate thickness and across the specimen section, producing a complete separation of the specimen (Fig. 8b).

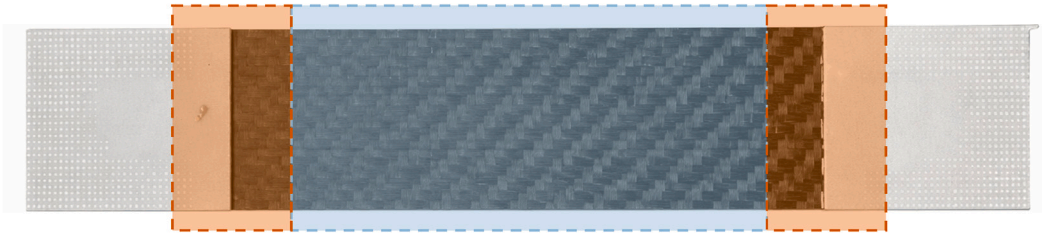

Fig. 6. Aerial schematic view of the specimen regions used for post-mortem fracture classification. Dominant gauge-region fracture morphologies were assigned when failure occurred within the blue region, while failures initiating or developing predominantly within the orange regions were classified as tab-influenced morphologies.

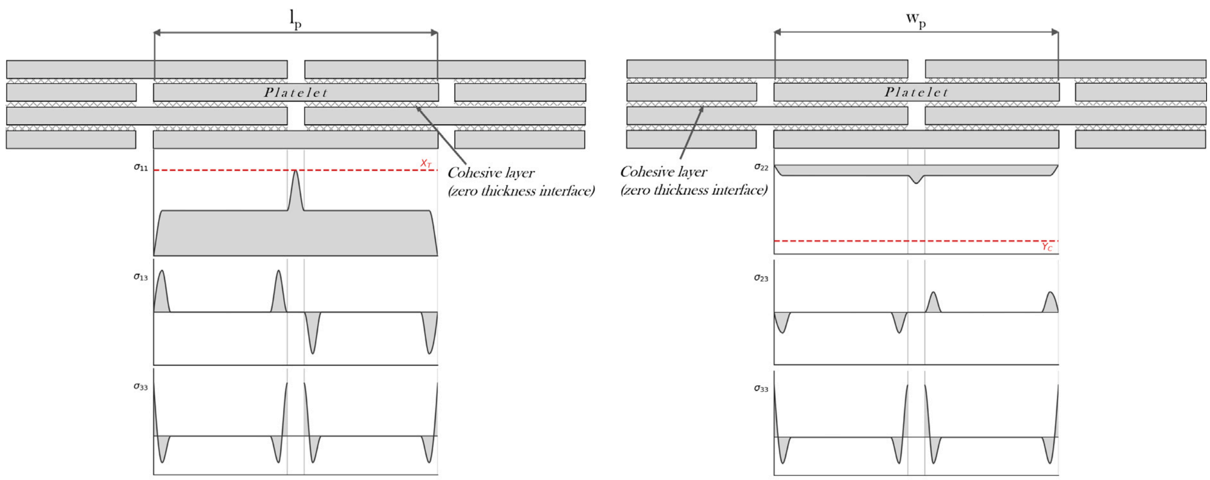

(a) Longitudinal stress state. (b) Transverse stress state.

Fig. 7. Schematic of the stress-transfer state in a woven EPP platelet under uniaxial tension. The schematic illustrates the platelet axial and transverse stresses (σ_{11} and σ_{22}), interlaminar shear stresses (σ_{13} and σ_{23}), and through-thickness peel stress (σ_{33}).

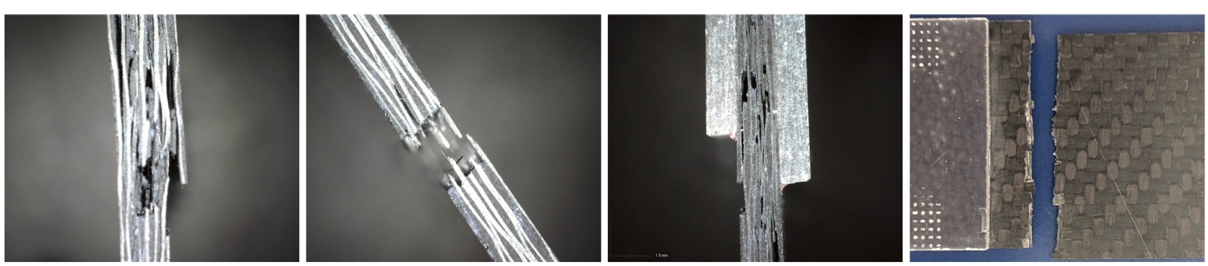

(a) Partial propagation (PP). (b) Full propagation (FP). (c) Partial propagation dominated by tab-influence (PP $-TI$). (d) Full propagation with tab-influenced partial propagation (FP $-TI$).

Fig. 8. Classification of failure modes.

In a subset of specimens, damage was observed near the end-tabs and were classified separately. These failures were not treated in the same manner as the gauge-region failure modes as the local boundary condition differed. The transition between the gripped tabbed section and the unsupported gauge section introduces a geometric and stiffness discontinuity. This can constrain lateral contraction, modify the local load-introduction path, and generate multiaxial stress concentrations involving longitudinal, transverse, shear, and peel stresses near the end-tab edge [38,39]. When these stress concentrations coincide with pre-existing inter-ply platelet discontinuities, damage may initiate, propagate, or arrest near the end-tab transition.

- **Partial propagation dominated by tab-influence** (PP $-$ TI): partial propagation observed primarily in the vicinity of the end-tabs, with damage initiation or arresting associated with the end-tab transition (Fig. 8c).
- **Full propagation with tab-influenced partial propagation** (FP $-$ TI): the specimen ultimately separated fully, but additional local delamination or partial propagation was observed near the end-tab transition region (Fig. 8d).

This classification was used as a post-mortem descriptor of the observed fracture morphologies rather than as a direct material property. In particular, the tab-influenced categories were not interpreted as pure

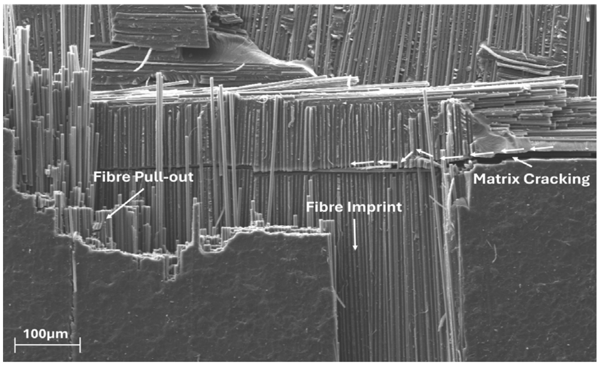

(a) Fibre pull-out, fibre imprints, and matrix cracking.

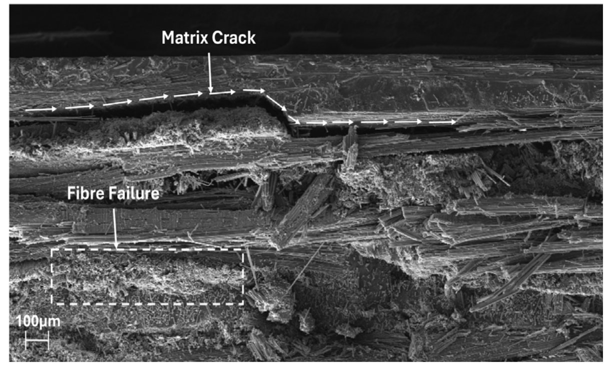

(b) Matrix crack propagation and fibre failure.

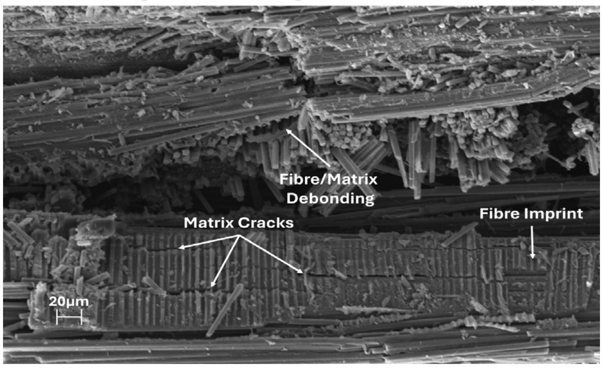

(c) Fibre/matrix debonding, matrix cracks, and fibre imprints.

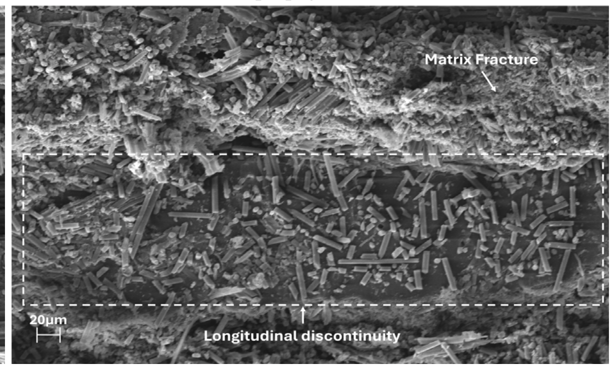

(d) Longitudinal discontinuity and matrix fracture.

Fig. 9. Representative SEM observations of local fracture mechanisms in woven EPP specimens. The annotated features show matrix cracking, fibre/matrix debonding, fibre pull-out, fibre imprints, and fibre failure.

intrinsic tensile failures, and instead as cases where the imposed specimen boundary condition interacted with the platelet architecture [39]. The classification was subsequently used to support the statistical interpretation of the tensile data and to distinguish any end-tab behaviour from architecture–property relationships.

The SEM observations, Fig. 9, provide evidence of the local microscopic fracture mechanisms active within the woven EPP fracture surfaces. Matrix cracking was observed in resin rich regions and propagating along platelet-to-platelet interfaces, indicating local matrix-dominated fracture during crack propagation and interfacial failure. Fibre imprints and fibre pull-out supporting fibre/matrix debonding, where fibres were separated from the surrounding matrix during fracture.

These features show that the macroscopic failure classifications result from interacting matrix, interface, and fibre-scale damage mechanisms. Partial-propagation morphologies are consistent with fracture surfaces showing fibre pull-out and fibre/matrix debonding, which can dissipate energy while delaying crack propagation. Full-propagation morphologies are consistent with the development of a continuous fracture path involving matrix cracking and fibre failure.

2.5. Analysis of variance

In order to statistically analyse the effects of the DoE factors (n_l, n_w, δ_l, δ_w and n_p) on the response variables (E, *UTS* and ε_f) the analysis of variance (*ANOVA*) was adopted and is outlined in Section 4.

The ANOVA modelling and the responses are based on multivariate linear regression [40]:

$$\mathbf{Y} = \mathbf{X}\boldsymbol{\beta} + \boldsymbol{\varepsilon} \tag{6}$$

where $\mathbf{Y}$ is a column vector containing the n observations of one of the response variables; $\mathbf{X}$ is the design matrix containing a column vector of ones (for intercept computation) and the k column vectors corresponding to the factor levels for each observation ($\mathbf{X} = \begin{bmatrix}\mathbf{1} & \mathbf{x}_1 & \mathbf{x}_2 & \dots & \mathbf{x}_k\end{bmatrix}$); $\boldsymbol{\beta}$ is the column vector containing the $p = k + 1$ regression coefficients, representing the effects of factors on the response variables; the model is thus linear in the coefficients $\boldsymbol{\beta} = \begin{bmatrix}\beta_0 & \beta_1 & \beta_2 & \dots & \beta_k\end{bmatrix}^T$; $\boldsymbol{\varepsilon}$ is the column vector containing the model errors with respect to the n response observations.

Following the motivation discussed in Section 1, different model formulations were adopted. Predictive models were implemented according to the following form:

$$y = \beta_0 + \beta_1 n_l + \beta_2 n_w + \beta_3 \delta l + \beta_4 \delta w + \beta_5 n_p + \varepsilon \tag{7}$$

where y is either E, *UTS* or ε_f; β_i are the model coefficients and ε is the error term. Moreover, an additional form for predictive models was implemented through the normalisation of the response variable:

$$y_n = \beta_0 + \beta_1 n_l + \beta_2 n_w + \beta_3 \delta l + \beta_4 \delta w + \beta_5 n_p + \varepsilon \tag{8}$$

where y_n is the normalised response, i.e., either E/n_p, UTS/n_p or ε_f/n_p. The purpose of this normalisation is to separate thickness-related scaling effects observed in the post-mortem analysis. These models are referred to as *predictive*, as the used factors are all design parameters, and can be used to determine the performance of platelet arrangements without their corresponding experimental dataset.

Interpretative models followed the following form:

$$y = \beta_{0,f_m} + \beta_1 n_l + \beta_2 n_w + \beta_3 \delta l + \beta_4 \delta w + \beta_5 n_p + \varepsilon \tag{9}$$

or:

$$y_n = \beta_{0,f_m} + \beta_1 n_l + \beta_2 n_w + \beta_3 \delta l + \beta_4 \delta w + \beta_5 n_p + \varepsilon \tag{10}$$

where the added categorical failure mode factor, f_m, represents an interpretation of the various failure modes discussed in Section 2.4. Four categories of f_m were assigned, corresponding to the observed failure modes in Section 2.4:

- Full-propagation failure modes (FP);
- Partial propagation failure modes (PP);
- Full propagation failure modes with observed partial propagation due to tab-influence (FP-TI);
- Partial propagation failure resulting from tab-influence (PP-TI).

The incorporation of f_m allows the model to compute a separate β_{0,f_m} for each observed failure mode. These models are referred to as *interpretative*, because the f_m factor can be derived only after a tensile test of the specimen. Therefore, they could only be utilised to better capture the variability of the platelet arrangement performances once experimental datasets have been produced. As such, they provide only hints regarding the interpretation of the behaviour of the platelet arrangements.

To estimate the unknown regression coefficients, the sum of the squared errors L of the model must be specified, Eq. (11):

$$L = \boldsymbol{\varepsilon}^T \boldsymbol{\varepsilon} = (\mathbf{y} - \mathbf{X}\boldsymbol{\beta})^T (\mathbf{y} - \mathbf{X}\boldsymbol{\beta}) \tag{11}$$

Minimising L with respect to $\boldsymbol{\beta}$, leads to estimation of the coefficients $\hat{\boldsymbol{\beta}}$, Eq. (12):

$$\left.\frac{\partial L}{\partial \boldsymbol{\beta}}\right|_{\hat{\boldsymbol{\beta}}} = 0 \rightarrow \hat{\boldsymbol{\beta}} = \left(\mathbf{X}^T\mathbf{X}\right)^{-1} \mathbf{X}^T \mathbf{y} \tag{12}$$

Based on this linear model assumption, the *ANOVA* tests the following null hypotheses:

$$H_0: \quad \mathbf{X}\boldsymbol{\beta} = 0 \tag{13}$$

against:

$$H_1: \quad \mathbf{X}\boldsymbol{\beta} \neq 0 \tag{14}$$

Meaning that if at least one element of $\boldsymbol{\beta}$ cannot be considered statistically equal to zero (i.e., therefore $\exists j \ : \ \beta_j \ \neq \ 0$), the null hypothesis H_0 can be refused with a certain confidence α.

For such a purpose, the Fisher's statistics F (Eq. (15)) and the associated p-value p can be calculated for each variability source in the model j.

$$F_j = \frac{Adj.MS_j}{Adj.MS_e} \tag{15}$$

where e stands for the error term. When testing the whole model, j can be set to r for regression. $Adj.MS_j$ stands for the *adjusted mean squares* corresponding to factor j. $Adj.MS_j$ is defined as $Adj.SS_j/DF_j$. $Adj.SS_j$ is the *adjusted sum of squares* (or type III correction of the sum of squares) for the jth factor; $Seq.SS_j$ is instead the *sequential sum of squares* (or type I sum of squares). DF_j stands for the degrees of freedom associated to the variability source. The ratio $Seq.SS_j/Seq.SS_t$, where t stands for total, gives the *contribution* of factor j in the description of data variability in percentage. To perform an assessment of the null hypothesis H_0, the corresponding p_j were computed.

3. Results

This section begins by outlining the measured tensile properties of the investigated architectures and arrangements, Table 3. The tensile test results, grouped by the number of plies, are then reported. In the following section, *ANOVA* is used to quantify and interpret the effects of the DoE factors on the response variables.

3.1. 4-Ply platelet arrangements

The tested 4-ply platelet arrangements and their tensile properties are highlighted in Fig. 10. All 4-ply EPP arrangements exhibited a predominantly linear response with an abrupt failure, consistent with the brittle macroscopic behaviour expected for woven CFRP laminates, with a representative stress–strain curve being illustrated in Fig. 11. However, the measured *UTS*, E, and ε_f varied substantially with platelet dimensions and superposition parameters. This supports the observation that the architecture modifies not only the failure properties, but the efficiency of the elastic load-transfer path.

For a 4-ply laminate, the amount of available through-thickness load-transfer paths is limited. Consequently, each platelet discontinuity, overlap, and matrix filled inter-ply region has a proportionally larger effect on the global response than in a thicker laminate. Under uniaxial tensile loading, axial stress, σ_{11}, must be transferred between discontinuous platelets through interlaminar shear stresses, σ_{13}, over the bonded regions. Woven EPPs further complicate this mechanism with a transverse reinforcement and corresponding transverse discontinuities, which results in σ_{22} and σ_{23}, while local peel stresses, σ_{33}, develop at platelet edges and overlap transitions. Therefore, an architecture's response should be interpreted as a result of a three-dimensional stress-transfer network, instead of a simple one-dimensional or two-dimensional overlap effect.

A useful comparison is provided by EPP #18 and #22, which share identical platelet dimensions (23.0×45.0 mm) and transverse superposition (δw = 25%), but differ in longitudinal superposition (δl = 50% for #18, and δl = 25% for #22). Reducing δl results in a notable increase in mean UTS from 306 MPa to 380MPa while the Young's modulus, E, moderately changes from 90.8 GPa to 88.3 GPa. This suggest that, for this architectural family, the dominant influence of δl was not elastic stiffness development, but the location and severity of the critical fracture path. The smaller longitudinal superposition in EPP #22 disperses the critical inter-ply discontinuities along the loading direction, removing the possibility that the platelet discontinuities could align through the thickness for a 4-ply arrangement. For asymmetric overlap configurations, the structural response is governed by the weakest stress-transfer path, being the smaller overlap segment [41]. However, the asymmetrical overlap architectures promoted a more distributed stress-transfer path and delayed unstable crack propagation, whereas the δl = 50% architecture of #18 concentrated the load transfer over fewer repeated overlap segments, increasing the local interfacial shear at critical platelet-to-platelet interfaces.

The coupled influence of longitudinal and transverse superposition is more clearly observed by comparing EPP #24, #26, #28, and #30. These architectures all use the same platelet dimensions (23.0 mm × 15.0 mm), but differ in δl and δw. The sharp decrease in *UTS* from EPP #24 to EPP #26, from 430 MPa to 295 MPa, occurred when the transverse superposition was reduced from 50% to 25%, while δl remained at 50%. This reduction in transverse overlap reduces the bonded area while also changing the spatial distribution of the transverse load-transfer network. A smaller transverse overlap length introduces a greater quantity of effective platelet edges and shorter bonded regions over which σ_{22}, σ_{23}, and σ_{33} can be equilibrated. Therefore, although the interlaminar shear is distributed over more transverse discontinuities, each overlap length is less effective at smoothing the local stress field, promoting local concentrations of σ_{23} and σ_{33} at platelet width edges, with associated perturbations to the longitudinal σ_{11} and σ_{13} shear-lag fields.

This comparison also illustrates why the effects of δl and δw are not simply linear. EPP #24 and #26 differ only in transverse superposition, however, their stiffness trends are inverse to their strength trends. EPP #24 exhibited a low modulus of 61.1 GPa, whereas EPP #26 had a modulus of 84.0 GPa. A stiffer initial response can arise from a more direct axial load path, however, it does not imply greater damage tolerance. In woven EPPs, the elastic response is governed primarily by the efficiency with which σ_{11} is developed and transferred through the platelet network. Meanwhile, *UTS* is governed by whether the local stress-transfer regions can tolerate the coupled interlaminar shear and peel stresses developed at the platelet edges. Therefore, an architecture may exhibit a higher apparent stiffness while failing at a lower ultimate stress if the discontinuity pattern generates sharper local σ_{13}, σ_{23}, or σ_{33} concentrations, or if it disturbs and affects the σ_{11} shear-lag field in a way that promotes unstable crack propagation. This stiffness–strength

Table 3
Tensile test results. *Order* is the manufacturing and testing order; $\overline{UTS}$ is the average ultimate tensile strength; s_{UTS} is the *UTS* standard deviation; $\overline{E}$ is the average Young's modulus; s_E is the Young's modulus standard deviation; $\overline{\varepsilon_f}$ is the average strain at failure; s_{ε_f} is the strain at failure's standard deviation; f_m is the dominant failure mode for the EPP arrangement.

ID	*Order*	$\overline{UTS}$	s_{UTS}	$\overline{E}$	s_E	$\overline{\varepsilon_f}$	s_{ε_f}	f_m
–	–	[MPa]	[MPa]	[GPa]	[GPa]	[mm/mm]	[mm/mm]	–
0	113–116	302.3	10.0	89.9	5.2	0.00353	0.00025	FP
1	53–56	315.3	15.1	96.8	3.8	0.00349	0.00012	PP-TI
2	105–108	295.6	11.7	85.8	1.6	0.00404	0.00025	FP
3	81–84	336.1	3.4	97.6	3.2	0.00404	0.00017	PP-TI
4	61–64	430.3	6.3	95.7	3.8	0.00486	0.00012	FP
5	13–16	539.1	20.7	68.1	1.0	0.01197	0.00078	PP-TI
6	9–12	422.1	18.3	88.4	3.4	0.00515	0.00029	PP-TI
7	41–44	440.6	12.7	99.8	2.7	0.00537	0.00048	FP
8	29–32	452.1	17.2	63.5	2.9	0.00893	0.00102	PP-TI
9	77–80	485.0	14.0	68.3	1.0	0.01017	0.00049	FP
10	69–72	454.5	20.8	63.5	1.4	0.00881	0.00074	FP-TI
11	109–112	313.8	9.3	97.4	3.8	0.00352	0.00017	PP-TI
12	121–124	416.9	31.9	94.9	4.3	0.00479	0.00048	PP-TI
13	117–120	456.3	16.7	99.8	4.2	0.00564	0.00070	FP
14	101–104	443.0	13.8	94.4	2.9	0.00534	0.00036	PP-TI
15	65–68	556.0	19.9	70.4	0.6	0.01196	0.00066	FP
16	97–100	280.2	9.6	86.0	1.3	0.00364	0.00032	PP-TI
17	17–20	302.0	10.4	88.9	1.0	0.00366	0.00028	PP-TI
18	37–40	305.7	9.5	90.8	5.0	0.00361	0.00018	PP-TI
19	93–96	308.0	5.8	93.4	2.4	0.00362	0.00025	PP-TI
20	73–76	350.7	20.9	90.4	4.3	0.00457	0.00050	FP
21	25–28	396.4	19.2	96.5	3.3	0.00479	0.00058	PP-TI
22	89–92	379.8	3.7	88.3	3.4	0.00487	0.00037	FP
23	5–8	417.6	8.5	94.2	4.7	0.00559	0.00021	FP
24	49–52	430.1	9.5	61.1	2.3	0.00860	0.00081	FP
25	21–24	453.7	20.5	66.4	0.5	0.00948	0.00098	FP-TI
26	129–132	294.7	11.8	84.0	4.5	0.00395	0.00024	FP
27	125–128	316.2	8.4	94.0	1.3	0.00381	0.00023	FP
28	57–60	454.4	28.6	69.6	0.7	0.00774	0.00056	FP
29	45–48	424.7	18.2	68.4	0.3	0.00772	0.00079	FP
30	85–88	411.9	19.7	67.2	1.1	0.00715	0.00041	FP
31	33–36	446.3	7.4	67.6	1.5	0.00965	0.00034	FP
32	1–4	247.7	1.6	90.5	3.8	0.00282	0.00017	FP

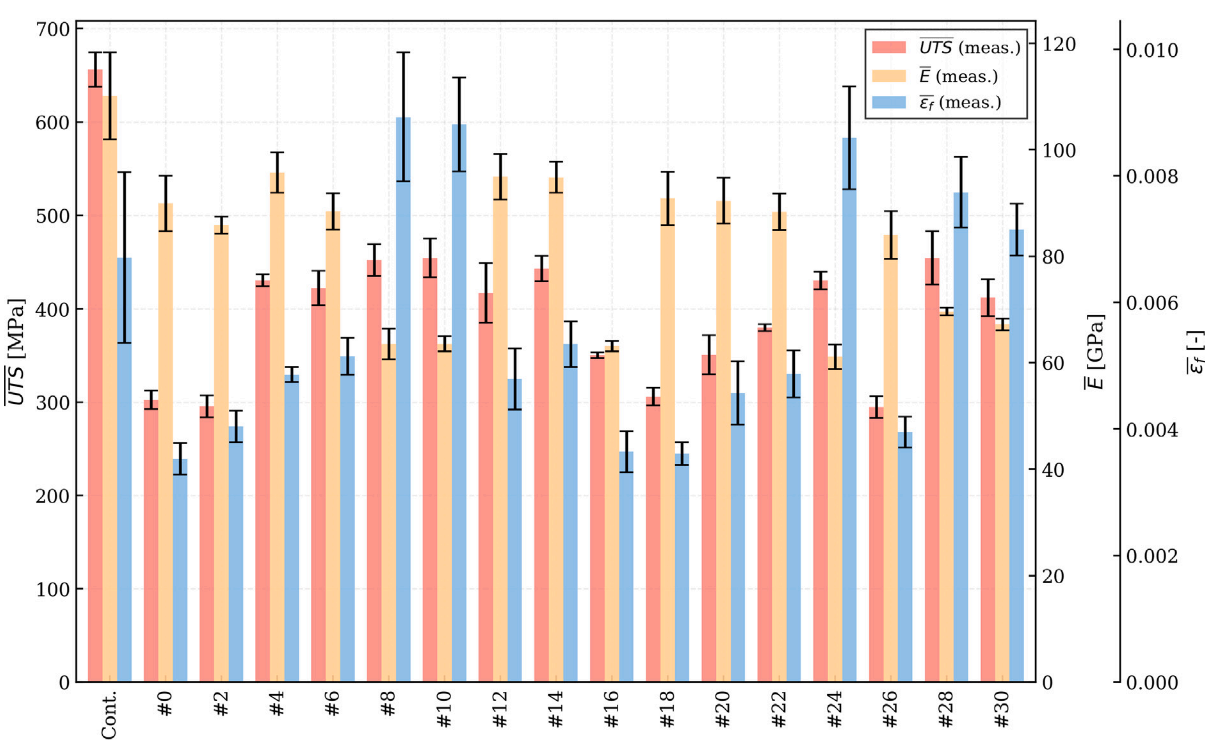

Fig. 10. 4-ply platelet arrangement uniaxial tensile test results, including: ultimate tensile strength $\overline{UTS}$ [MPa]; young's modulus $\overline{E}$ [GPa]; and strain at failure $\overline{\varepsilon_f}$ [−]. *Cont.* corresponds to the reference continuous woven specimens, while # corresponds to a platelet arrangement ID in Table 1.

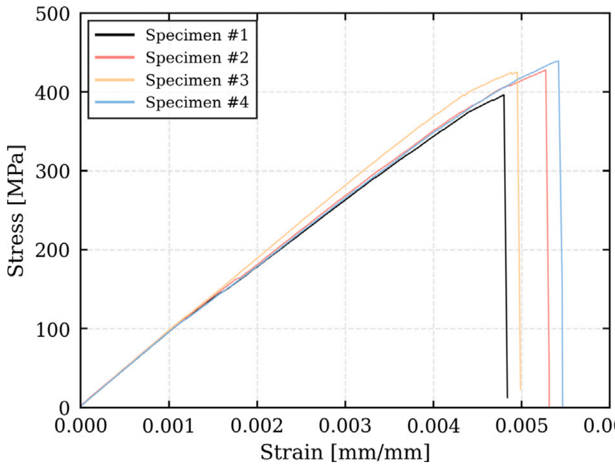

Fig. 11. A 4-ply platelet arrangement stress–strain curve (EPP #6).

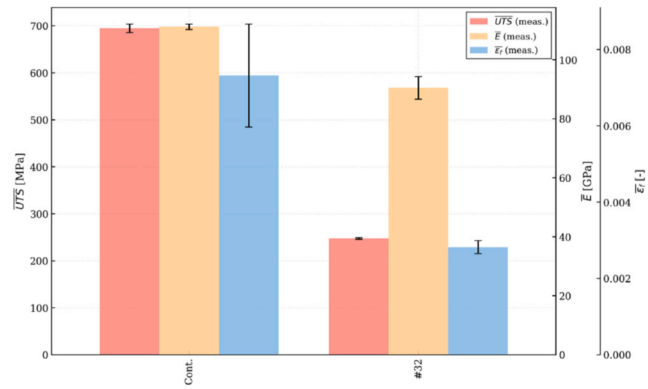

Fig. 12. 6-ply platelet arrangement uniaxial tensile test results, including: ultimate tensile strength $\overline{UTS}$ [MPa]; young's modulus $\overline{E}$ [GPa]; and strain at failure $\overline{\epsilon_f}$ [−]. *Cont.* corresponds to the reference continuous woven specimens, while # corresponds to a platelet arrangement ID in Table 1.

decoupling is consistent with observations by Ko et al. [31], who observed that platelet width and width overlap can strongly influence the tensile strength and modulus by impacting a platelet system's shear-lag efficiency.

The behaviour of EPP #28 and #30 further supports this interpretation. These arrangements retain reduced longitudinal superpositions, but their UTS values remained higher than that of #26. In these cases, the reduced δl modifies the spacing of the longitudinal overlaps and distributed the longitudinal discontinuities more broadly along the gauge length. When combined with the transverse discontinuity pattern, this can prevent a single overlap transition from becoming the dominant fracture path. Therefore, the spatial arrangement of the smallest bonded overlap regions and inter-ply regions between adjacent platelets become the relevant descriptors alongside δl and δw. In 4-ply architectural arrangements, where few alternative load-transfer bridges exist through the laminate thickness, this spatial arrangements affects whether damage remains distributed and resulting in interfacial failure or collapses into a full-propagation failure.

In addition, influence of platelet length can be interpreted through α and L_C. For the present material system, all longitudinal and transverse overlap lengths were greater than the calculated L_C, indicated that the investigated architectures were not necessarily governed by insufficient transfer-length. Particularly, the available overlap lengths were sufficient, in principle, for substantial axial stress to develop within the platelets before interfacial failure would dominate. This helps explain why altering l_p does not produce a monotonic change in the tensile properties, however, exceeding L_C does not eliminate the influence of platelet length. Reducing l_p increases the number of longitudinal discontinuities and increases the number of platelet edges within the gauge region, increasing the number of potential sites for local σ_{13}, σ_{33}, and matrix/interfacial damage initiation. Meanwhile, increasing l_p reduces the number of discontinuities while concentrating the load-transfer into fewer overlap transitions. Therefore, once the critical length conditions is satisfied, the role of platelet length shifts from enabling axial stress development to controlling the density, spacing, and interaction of discontinuities.

The effect of platelet width is similarly architecture-dependent. Wide platelets (w_p = 45.0 mm) provide a larger transverse bonded region and reduce the number of platelet-width edges within the specimen width, resulting in fewer interfacial stresses along the longitudinal load path. This can stabilise the transverse stress-transfer field by reducing the frequency of σ_{23} and σ_{33} concentrations associated with transverse discontinuities. Meanwhile, narrow platelets (w_p = 15.0 mm) increase the number of transverse discontinuities, introducing more inter-ply regions where σ_{22}, σ_{23}, and σ_{33} must be equilibrated locally. Depending on the longitudinal architectural parameters, this does not necessarily heavily penalise the structural response. If the overlap topology is capable of distributing these discontinuities without creating a dominant through-thickness fracture path, the greater quantity of platelet edges and discontinuities can promote distributed damage, fibre pull-out, bridging, and higher apparent failure strain. However, if the reduced width or transverse overlap concentrates σ_{23} and σ_{33} along a longitudinal discontinuity, the same narrow-platelet architecture can become more sensitive to unstable delamination or FP failure.

The post-mortem fracture analyses support these observations, with arrangement classified with FP failure corresponding to cases where a dominant crack path was formed through the platelet network, producing a complete separation of the specimen once the local fracture resistance of an inter-ply region was exceeded. Meanwhile, PP cases indicate that crack growth was arrested or deflect by localised delamination, fibre pull-out, or bridging, retaining residual continuity after peak load. Meanwhile tab-influenced morphologies followed a similar failure, with the additional multiaxial stress concentrations caused by the end-tab transition interacting with nearby platelet edges and discontinuities.

Overall, the results emphasise that the woven EPP tensile performance is governed by the stability of the three-dimensional load-transfer network. Since all overlap lengths exceeded the platelet critical length, the observed differences are not attributed to insufficient transfer-length regimes. Instead, longitudinal overlaps control the spacing and severity of axial shear-lag transfer regions, while transverse overlaps control the distribution of transverse stress-transfer and platelet edge stress concentrations while the platelet dimensions and superposition determine the density and spatial arrangement of the matrix rich discontinuities. The resulting tensile response is governed by the combined influence of the architectural parameters l_p, w_p, δl, δw and their influence of σ_{11} development, interlaminar shear concentration, peel stress development, and the ability of the architecture to redistribute load once matrix crack initiation and propagation occur.

3.2. 6-Ply platelet arrangement

The 6-ply platelet architecture (EPP #32) was introduced as a central point to probe potential curvature in the DoE response. Consequently, unlike the 4-ply or 8-ply platelet arrangements, only a single 6-ply EPP architecture was manufactured and tested. A single discontinuous architecture does not support within-group comparisons to isolate the effects of the various DoE factors. The 6-ply EPP architecture can therefore be interpreted primarily relative to the continuous 6-ply baseline. The architecture's tensile properties are highlighted in Fig. 12.

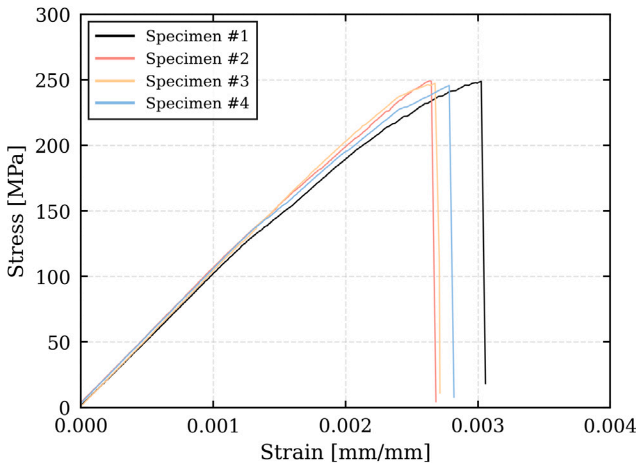

Fig. 13. 6-ply platelet arrangement stress–strain curve of EPP #32.

Qualitatively, EPP #32 retains a brittle failure response (Fig. 13), but fails at a substantially lower UTS and ε_f compared to the continuous (247.7 MPa and 0.00282 mm/mm, respectively). Despite being a balanced architecture with regards to overlap superpositions, the central superpositions of 33.3% penalise strength and strain far more than stiffness.

3.3. 8-Ply platelet arrangements

The tested 8-ply platelet architectures and their overall tensile properties are highlighted in Fig. 14.

The tensile response of the 8-ply EPP arrangements remained predominantly brittle, consistent with the corresponding 4-ply arrangements, but exhibiting clearer development of progressive ply failure, Fig. 15. Across several arrangements, a reduction in tangent stiffness was observed at $\varepsilon \approx 0.004$ mm/mm, indicating the onset of distributed damage or progressive ply failure prior to ultimate failure. This response was also observed in the continuous woven reference specimens and was verified not to originate from instrumentation artefacts. Unlike the 4-ply arrangements, where the limited quantity of through-thickness load-transfer paths increases the sensitivity to individual discontinuities or localised heterogeneity, the 8-ply arrangements provide additional platelet interfaces and redundant load-transfer bridges. This improves the architecture's capacity for stress redistribution after local matrix cracking or interfacial damage initiates. The observed stiffness reduction is therefore interpreted as the initiation of local damage and stress redistribution within the laminate, consistent with the role of thickness in discontinuous fibre composites, where increasing the number of platelet layers increases the effective fracture process zone, reducing sensitivity to individual meso-scale defects [31].

Direct comparisons between equivalent 4-ply and 8-ply arrangements highlight the influence of ply count, n_p, on the stability of the load-transfer network. EPP #23 corresponds to the same architecture as the 4-ply EPP #22, retaining a similar global stress–strain response while exhibiting an increase in E and UTS of approximately 7% and 10%, respectively. Likewise, EPP #7 exhibited an approximate 12% increase in E and 4% increase in UTS relative to the corresponding 4-ply arrangement, EPP #6, while retaining the same final fracture morphology. These trends indicate that increasing n_p does not merely scale the laminate response through the added thickness. Instead, the additional plies increase the number of possible load-transfer paths across platelet discontinuities, allowing local σ_{13}, σ_{23}, and σ_{33} concentrations to be redistributed through adjacent interfaces before fracture occurs. This thickness effect can also be interpreted in terms of an effective Fracture Process Zone (FPZ), defined here as the meso-scale region ahead of the dominant crack path in which matrix cracking, platelet-to-platelet debonding, delamination, fibre pull-out, and local bridging can develop prior to complete specimen failure. Increasing n_p increases the number of platelet interfaces and adjacent load-transfer paths available within this region, allowing local damage to redistribute through the laminate rather than immediately forming a dominant through-thickness crack or delamination. Consequently, the thicker 8-ply arrangements are less sensitive to singular platelet discontinuities, interlaminar defects, and platelet heterogeneity while exhibiting an apparent resistance to localisation.

Architecture-driven differences remain significant in the 8-ply arrangements, particularly when platelet width and overlap balance are varied. Platelet width and laminate thickness affect the tensile properties and scatter through their influence on stress-transfer efficiency and damage development. In the present EPPs, narrow platelet arrangements introduce a greater number of transverse discontinuities, resulting in more locations where σ_{22}, σ_{23}, and σ_{33} must be equilibrated. This can promote a more distributed damage when the overlap topology prevents a dominant fracture path or arrests damage propagation, but it can also increase sensitivity to local stress concentrations if the transverse interfacial stresses interact with the longitudinal stress-field, especially when they coincide unfavourably through the thickness. The greater scatter in tensile properties observed for the narrow-width families in Fig. 14 is consistent with the stronger dependence on local platelet-to-platelet stress redistribution.

The influence of overlap balance is illustrated when comparing EPP #13 and #11. Both use 34.5×15.0 mm platelets, but differ in their superposition parameters: $\delta l/\delta w = 25\%/50\%$ for #13 compared to $50\%/25\%$ for #11. The resulting difference in average UTS is substantial, with $UTS = 456.3$ MPa for #13 compared with 313.8 MPa for #11. Meanwhile, the stiffness varied minimally, with 99.8 GPa and 97.4 GPa, respectively. This indicates that both arrangements were able to develop an efficient initial longitudinal load path, but differed markedly in their resistance to unstable fracture. The larger transverse superposition in EPP #13 reduces the quantity of local σ_{23} and σ_{33} concentrations at the platelet width edges, while the reduced longitudinal superposition distributes the longitudinal discontinuities more broadly along the loading direction resulting fewer peak axial stresses in the adjacent platelets over those longitudinal discontinuities. This combination appears to the delay the formation of a dominant through-thickness fracture path. In contrast, EPP #11 combines a reduced transverse superposition with a larger longitudinal superposition, with the former increasing local interlaminar stresses in the transverse direction. Despite the transverse stresses being significantly lower than the longitudinal stresses, the coupled σ_{11}, σ_{13}, σ_{23}, and σ_{33} stress state is more severe with the larger δl grouping longitudinal discontinuities into fewer longitudinal locations.

Across the 8-ply arrangements, architectures $\delta l = 25\%$ more consistently displayed a staged progressive failure sequence and higher apparent damage tolerance, whereas several $\delta l = 50\%$ arrangements trended toward more abrupt failure. In 8-ply laminates, the greater number of interfacial interfaces provides additional paths for redistributing local σ_{13}, σ_{23}, and σ_{33} stress concentrations, making the transition between stable stress redistribution and unstable localisation of damage more dependent on the three-dimensional arrangement of the platelets, overlap topology, and the resulting bonded areas.

Overall, the 8-ply arrangements achieved systematically higher tensile properties than their 4-ply counterparts, confirming that additional plies strengthen the internal load-transfer network and improve an architecture's resistance to localised effects. However, the improvement is architecture-dependent rather than purely thickness-driven. The added plies reduce the relative influence of the unbalanced outer plies, increase the number of neighbouring interfaces available for shear redistribution, reduce the sensitivity to localised heterogeneity and defects, and enlarge the effective FPZ over which damage can occur and propagate prior to failure.

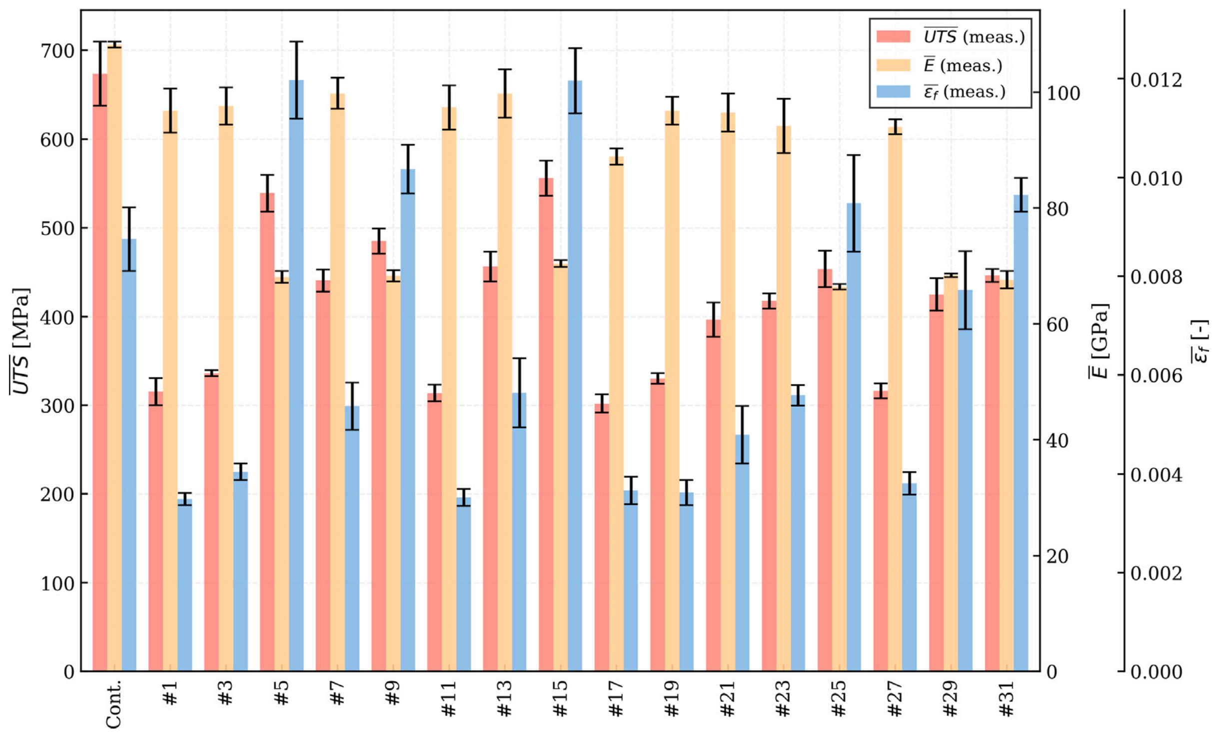

Fig. 14. 8-ply platelet arrangement uniaxial tensile test results, including: ultimate tensile strength $\overline{UTS}$ [MPa]; young's modulus $\overline{E}$ [GPa]; and strain at failure $\overline{\varepsilon_f}$ [−]. *Cont.* corresponds to the reference continuous woven specimens, while # corresponds to a platelet arrangement ID in Table 1.

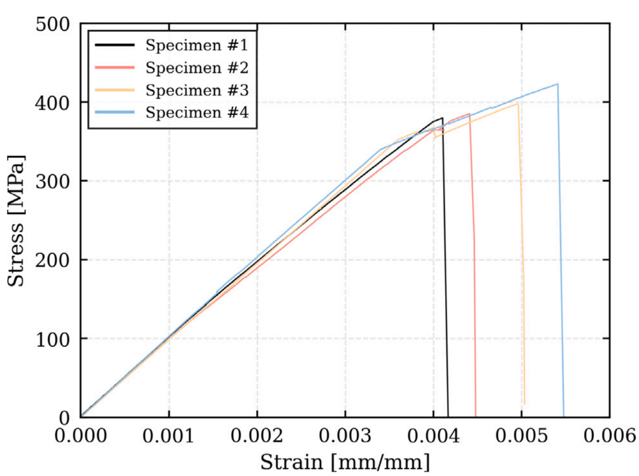

Fig. 15. An 8-ply platelet arrangement stress–strain curve (EPP #21).

4. Discussion

In this section, the results regarding the *ANOVA* of different models for the tensile responses are reported. The agreement and fit of the adopted models is discussed alongside the interpretation of the results.

Specimens associated with Tab-Influenced fracture morphologies were retained in the ANOVA dataset. A comparative analysis excluding the FP-TI and PP-TI specimens produced no substantive change in the model trends, coefficient interpretation, or R^2_{adj} values, and was therefore retained to preserve the complete experimental characterisation.

4.1. First order predictive models

This section implements models of the kind in Eq. (7). These were the simplest models that could be built and the easiest to interpret, but

Table 4
R^2 coefficient variants related to the first order model for the response variables (Resp. Var.). R^2 is the traditional coefficient; R^2_{adj} is the adjusted R^2; R^2_{pred} is the prediction R^2.

Resp. Var.	S	R^2	R^2_{adj}	R^2_{pred}
E	10.8809	34.13%	31.51%	27.61%
UTS	54.1986	54.25%	54.44%	50.52%
ε_f	0.00217478	34.63%	32.03%	28.45%

the most critical models in terms of description of data variability. The three model equations are reported in Eqs. (16), (17), and (18), whereas the associated R^2 values are reported in Table 4.

$$E\,[\text{GPa}] = 93.91 - 2.101n_l - 6.878n_w + 0.823\delta l + 2.263\delta w + 0.847n_p \tag{16}$$

$$UTS\,[\text{MPa}] = 306.8 - 21.45n_l + 30.86n_w + 41.90\delta l - 10.86\delta w + 5.98n_p \tag{17}$$

$$\varepsilon_f\,[\#] = 0.00280 - 0.000287n_l + 0.001264n_w + 0.000634\delta l - 0.000410\delta w + 0.0002328n_p \tag{18}$$

As shown, only the *UTS* model has a R^2_{adj} above 50%, whereas the other models obtain values of ∼34%. This means that the models are capable of describing only ∼34% of the variability in the associated response variable, while the remainder is composed of pure error or lack-of-fit. Discussing the effect of the DoE factors using these models is not useful, however, a conclusion that can be derived by this analysis is that the phenomenon underlying the platelet arrangements and their mechanics is far from being linear. The same is visible on the main effect plots, an example of which for E is shown in Fig. 16. Even the results on *UTS* require further modelling.

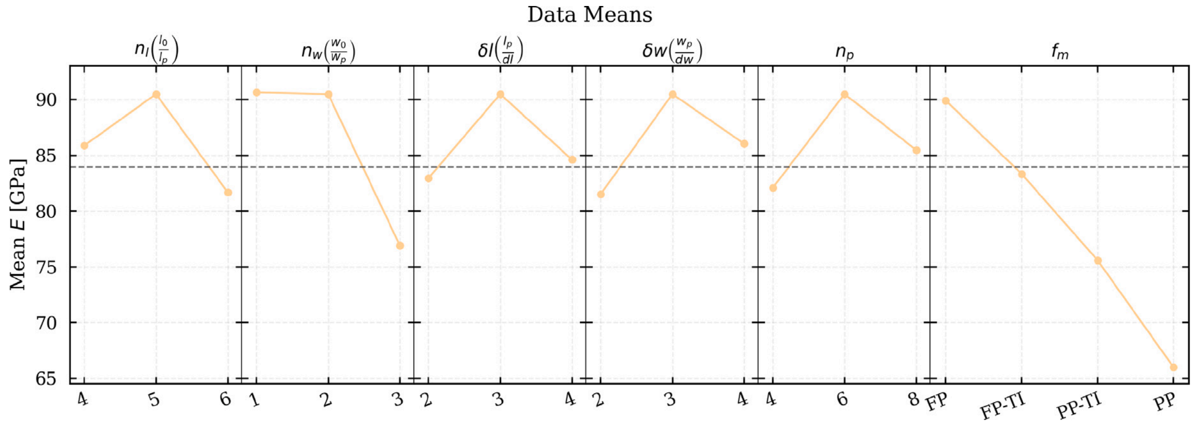

Fig. 16. Main effect plots of DoE factors (n_l, n_w, δ_l, δ_w and n_p) and the failure mode f_m on the composite's Young's Modulus, E.

Table 5
R^2 coefficient variants related to the first order model for the response variables (Resp. Var.), including the failure mode indicator f_m. R^2 is the traditional coefficient; R^2_{adj} is the adjusted R^2; R^2_{pred} is the prediction R^2.

Resp. Var.	S	R^2	R^2_{adj}	R^2_{pred}
E	8.20829	63.41%	61.03%	57.42%
UTS	44.2142	70.28%	68.35%	66.53%
ε_f	0.00159767	65.56%	63.32%	59.83%

4.2. First order interpretative models

This section implements models of the kind in Eq. (9). The failure mode variable f_m was found to be strongly correlated with the responses of the models, as shown in the main effects plot in Fig. 16. The addition of this variable to the analysis introduced a good amount of described variance in the models. The three model equations are reported in Eq. (19), (20), and (21), while their associated R^2 values are reported in Table 5.

$$\begin{aligned} E\,[\text{GPa}] &= \beta_{0,f_m} - 0.052n_l - 5.022n_w \\ &\quad +5.136\delta l + 1.782\delta w + 1.531n_p \\ \beta_{0,FP} &= 71.96 \qquad \beta_{0,FP-TI} = 62.69 \\ \beta_{0,PP} &= 50.09 \qquad \beta_{0,PP-TI} = 52.78 \end{aligned} \tag{19}$$

$$\begin{aligned} UTS\,[\text{MPa}] &= \beta_{0,f_m} - 28.02n_l + 22.88n_w \\ &\quad +23.65\delta l - 9.98\delta w + 3.24n_p \\ \beta_{0,FP} &= 389.2 \qquad \beta_{0,FP-TI} = 459.7 \\ \beta_{0,PP} &= 478.3 \qquad \beta_{0,PP-TI} = 465.7 \end{aligned} \tag{20}$$

$$\begin{aligned} \varepsilon_f\,[\#] &= \beta_{0,f_m} - 0.000681n_l \\ &\quad +0.000879n_w - 0.000257\delta l \\ &\quad -0.000326\delta w + 0.0000936n_p \\ \beta_{0,FP} &= 0.00719 \qquad \beta_{0,FP-TI} = 0.00952 \\ \beta_{0,PP} &= 0.01167 \qquad \beta_{0,PP-TI} = 0.01109 \end{aligned} \tag{21}$$

As shown, the variabilities described by the updated models were dramatically increased from ~32% to ~61%, for both E and ε_f. The UTS model achieved a R^2_{adj} of 68.35%, improving the model's descriptive abilities by 14%. As described previously, the f_m indicator is based on the failure mode of the specimen, therefore an increase in the R^2 coefficients for both UTS and ε_f was naturally expected. However, the improvement for the E model suggests that the stiffness response of the platelet architectures is closely coupled to the damage evolution and stress redistribution mechanisms, rather than being purely parameter driven. This reinforces the fact that the f_m factor is an important term to be considered, despite it not being applicable for a predictive model to pre-emptively determine platelet architecture performances. Nevertheless, this suggests that a modelling theory capable of discriminating between shear- and normal-stress driven elasticity can offer improve prediction capabilities. Since the R^2_{adj} coefficients are still low, it is still not fruitful to discuss the effects of the various DoE factors.

4.3. Normalised predictive models

This section considers the hypothesis suggested by the main effects plot trends that an appropriate normalisation of the responses may reduce non-linearity and lead to a linearisation of the effect of DoE factors. With half of the EPP architectures being repeated with additional plies, n_p, comparing tensile performance on a per-ply basis provides a more representative basis for assessing the influence of the EPP architecture itself and the DoE factors. Accordingly, the implemented adopted models followed the kind in Eq. (8).

This normalisation shifts the interpretation from absolute laminate performance to the average per-ply contribution to the E, UTS and ε_f. The added ply count modifies the mechanics of woven EPPs, altering the number of platelet interfaces, the degree of through-thickness constraint, and the average number of available neighbouring load-transfer paths around a discontinuity. In thinner laminates, unbalanced outer-ply peel stresses and matrix rich inter-ply regions have a proportionally larger influence on the global response than in thicker laminates, where additional internal plies more greatly allow local interlaminar shear stresses to redistribute through adjacent interfaces prior to forming cracks. Even more relevant for discontinuous systems, as increasing n_p modifies the FPZ, reducing the likelihood that damage within a single platelet discontinuity results in immediate damage propagation and failure. The strong effect of n_p observed in the first order models therefore reflects a thickness-dependent change in stress-transfer and damage-redistribution mechanisms.

This improvement obtained through normalisation is particularly evident for E/n_p, as highlighted by the associated main effects plot in Fig. 17. The introduction of normalisation further emphasised the influence of n_p on the EPP architecture and its mechanics, highlighting that a large proportion of non-linearity was primarily influenced by this parameter. The three model equations are reported in Eq. (22), (23), and (24), while their associated R^2 values are reported in Table 6.

$$\begin{aligned} \frac{E\,[\text{GPa}]}{n_p} &= 33.00 - 0.413n_l - 1.317n_w \\ &\quad +0.354\delta l + 0.327\delta w - 2.4592n_p \end{aligned} \tag{22}$$

$$\begin{aligned} \frac{UTS\,[\text{MPa}]}{n_p} &= 130.56 - 3.890n_l + 6.165n_w \\ &\quad +7.167\delta l - 1.787\delta w - 11.215n_p \end{aligned} \tag{23}$$

$$\begin{aligned} \frac{\varepsilon_f\,[\#]}{n_p} &= 0.001655 - 0.0000409n_l \\ &\quad +0.0002402n_w + 0.0000768\delta l \\ &\quad -0.0000659\delta w - 0.0001458n_p \end{aligned} \tag{24}$$

Compared to the first order counterparts presented in Section 4.1, the normalised models describe more of the variability in the data.

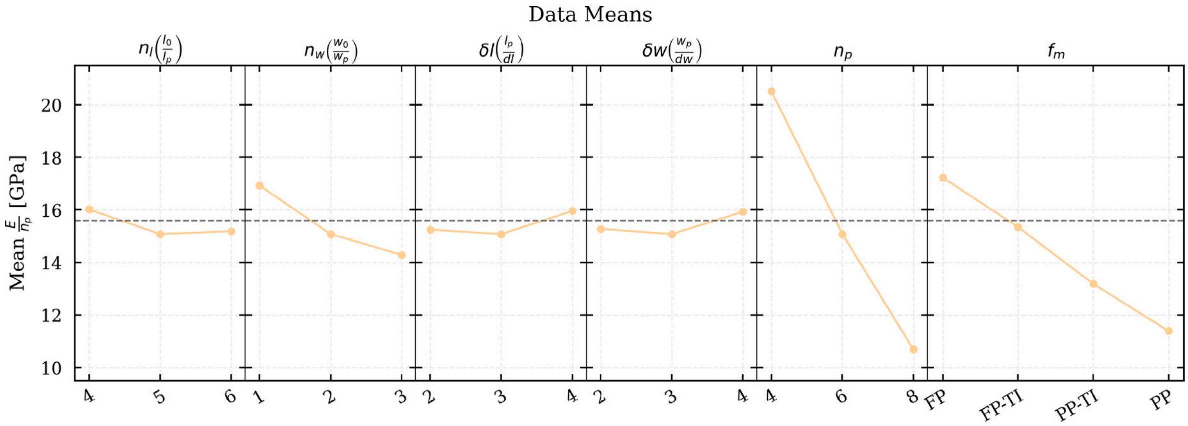

Fig. 17. Main effect plots of DoE factors (n_l, n_w, δ_l, δ_w and n_p) and the failure mode f_m on the composite's normalised Young's Modulus, E/n_p.

Table 6
R^2 coefficient variants related to the normalised model for the response variables (Resp. Var.). R^2 is the traditional coefficient; R^2_{adj} is the adjusted R^2; R^2_{pred} is the prediction R^2.

Resp. Var.	S	R^2	R^2_{adj}	R^2_{pred}
E	2.05915	86.32%	85.77%	84.95%
UTS	10.6417	84.57%	83.95%	83.37%
ε_f	0.000369459	53.51%	51.67%	49.20%

Specifically, the R^2_{adj} of E/np reached 85.77% compared to the first order model E of 31.51%, while the R^2_{adj} of UTS/n_p improved to 83.95% from 54.44%. However, the ε_f/n_p model has not drastically improved, retaining a low R^2_{adj} of 51.67%, which is still an improvement from the original 32.03%. This is consistent with the failure strain being more sensitive to local damage initiation, matrix crack propagation, and fracture processes than to the average elastic load-transfer efficiency alone.

The improved linearity of the normalised models confirms that thickness is a dominant source of apparent non-linearity regarding the absolute responses. Nevertheless, the persistence of a statistically significant n_p term in the normalised models highlights that each ply does not contribute independently or identically to the laminate response. Instead, the per-ply contribution changes with thickness as the through-thickness stress-transfer network, local interlaminar shear redistribution, surface ply peel stress contribution, and effective FPZ evolve as additional plies are introduced. With these improved R^2_{adj} values, factors effect interpretation becomes important. Interpretation is provided for elastic behaviour and effect on failure, with the support of the *ANOVA* tables in Table 7:

- n_l controls the platelet length, with an increasing n_l reducing l_p for the fixed gauge length l_0. This parameters exhibits a negative effect on all normalised response variables, reducing the per-ply contribution to the Young's modulus, *UTS*, and strain at failure. Increasing n_l results in a greater number of longitudinal discontinuities, and therefore platelet edges, increasing the number of inter-ply regions where local interlaminar stresses and interfacial damage can initiate. Since all tested overlap lengths exceeded the L_C, the negative influence of n_l should be interpreted with regards to its control over discontinuity density, spacing, and the interaction of stress-transfer discontinuities. The *p*-values associated with n_l are below 5% for E/n_p and UTS/n_p, indicating statistical significance for stiffness and strength, while its effect on ε_f/n_p is not statistically significant. This can be attributed to the fact that the matrix within the discontinuities are more ductile, however, the longitudinal discontinuities are too small to actively contribute to the elongation at failure.
- n_w controls the platelet width, with an increasing n_w reducing w_p for the fixed specimen width w_0. This parameter exhibits a negative effect on E/n_p, and a positive effect on UTS/n_p and ε_f/n_p. Increasing n_w increases the number of transverse discontinuities and platelet-width edges, introducing more locations where σ_{22}, σ_{23}, and σ_{33} must be equilibrated while introducing more transverse inter-ply regions along the loading direction, disrupting the longitudinal load-transfer pathway. However, the increased number of transverse discontinuities promotes more distributed damage, crack arresting, and fibre pull-out as the overlap topology prevents the formation of a dominant fracture path along the specimen's width. This coincides with the positive effect of n_w on the normalised failure-related responses. The associated *p*-values are close to 0%, indicating that the platelet width is a statistically significant parameters for all normalised responses.
- δl controls the longitudinal superposition between platelets in adjacent plies and therefore the topology of the axial shear-lag transfer path. The positive coefficients for all normalised response variables indicate that larger longitudinal superpositions improve the per-ply tensile response within the tested design space. Since all longitudinal overlap lengths are greater than L_C, δl controls the spacing, repetition, and interaction of longitudinal discontinuities along the loading direction. Larger δl increases the overlap continuity along the primary load-transfer direction, reducing the quantity of σ_{13} and σ_{33} disturbances to a platelet's axial stress distribution. The *p*-value for E/n_p is slightly above 5%, whereas for UTS/n_p and ε_f/n_p, δl has a stronger statistical influence regarding the failure-related responses.
- δw controls the transverse superposition between platelets in adjacent plies. Within the tested bounds, this factor has a smaller significance than the other DoE parameters, with the *p*-values marginally above or marginally below the 5% threshold depending on the response. This does not imply that the transverse overlap is mechanically irrelevant, as it affects the bonded area between adjacent platelets while controlling the spacing of transverse discontinuities that can perturb the longitudinal σ_{11} and σ_{13} shear-lag field. However, for this uniaxial tensile test, this parameter is comparatively weaker compared to the other DoE factors.
- n_p determines the number of plies within the platelet architecture and remains statistically significant for all normalised response variables. The negative coefficient indicates that increasing the laminate thickness reduces the average per-ply contribution, even though the absolute laminate properties generally increase. This confirms that the thickness effect is not monotonic, as additional interfaces and internal plies improve the through-thickness redistribution, enlarging the effective FPZ, while also reducing the laminate's sensitivity to longitudinal discontinuity positioning.

Table 7
ANOVA tables related to the normalised predictive models for the response variables (Resp. Var.). *Source* is the origin of the variance; *DF* are the degrees of freedom; *Seq. SS* is the sequential sum of squares, quantifying variability associated to factors in their order of appearance; *Contribution* explains the contribution in percentage; *Adj. SS* is the adjusted sum of squares; *Adj. MS* is the adjusted mean of sum of squares; *F-value* is the ratio between explained and error variabilities; *p-value* is the probability associated to the *F-value*.

Resp. Var.	Source	DF	Seq. SS	Contribution	Adj. SS	Adj. MS	F-value	p-value
	Regression	5	3370.04	86.32%	3370.04	674.01	158.96	0.000
	$n_l\,[\frac{l_o}{l_p}]$	1	21.87	0.56%	21.87	21.87	5.16	0.025
	$n_w\,[\frac{w_o}{w_p}]$	1	222.05	5.69%	222.05	222.05	52.37	0.000
E	$\delta l\,[\frac{l_p}{d_l}]$	1	16.07	0.41%	16.07	16.07	3.79	0.054
	$\delta w\,[\frac{w_p}{d_w}]$	1	13.70	0.35%	13.70	13.70	3.23	0.075
	n_p	1	3096.35	79.31%	3096.35	3096.35	730.26	0.000
	Error	126	534.25	13.68%	534.25	4.24		
	Lack-of-Fit	27	494.62	12.67%	494.62	18.32	45.76	0.000
	Pure error	99	39.64	1.02%	39.64	0.40		
	Total	131	3904.29	100.00%				
	Regression	5	78 177.9	84.57%	78 177.9	15 635.6	138.07	0.000
	$n_l\,[\frac{l_o}{l_p}]$	1	1936.5	2.09%	1936.5	1936.5	17.10	0.000
	$n_w\,[\frac{w_o}{w_p}]$	1	4865.0	5.26%	4865.0	4865.0	42.96	0.000
UTS	$\delta l\,[\frac{l_p}{d_l}]$	1	6574.2	7.11%	6574.2	6574.2	58.05	0.000
	$\delta w\,[\frac{w_p}{d_w}]$	1	408.7	0.44%	408.7	408.7	3.61	0.060
	n_p	1	64 393.4	69.65%	64 393.4	64 393.4	568.62	0.000
	Error	126	14 268.9	15.43%	14 268.95	113.2		
	Lack-of-Fit	27	13 250.6	14.33%	13 250.6	490.8	47.71	0.000
	Pure error	99	1018.3	1.10%	1018.3	10.3		
	Total	131	92 446.7	100.00%				
	Regression	5	0.000020	53.51%	0.000020	0.000004	29.01	0.000
	$n_l\,[\frac{l_o}{l_p}]$	1	0.000000	0.58%	0.000000	0.000000	1.57	0.212
	$n_w\,[\frac{w_o}{w_p}]$	1	0.000007	19.95%	0.000007	0.000007	54.08	0.000
ε_f	$\delta l\,[\frac{l_p}{d_l}]$	1	0.000001	2.04%	0.000001	0.000001	5.53	0.020
	$\delta w\,[\frac{w_p}{d_w}]$	1	0.000001	1.50%	0.000001	0.000001	4.07	0.046
	n_p	1	0.000011	29.44%	0.000011	0.000011	49.78	0.000
	Error	126	0.000017	46.49%	0.000017	0.000000		
	Lack-of-Fit	27	0.000016	43.96%	0.000016	0.000001	63.71	0.000
	Pure error	99	0.000001	2.53%	0.000001	0.000000		
	Total	131	0.000037	100.00%				

Table 8
R^2 coefficient variants related to the normalised model for the response variables (Resp. Var.), including the failure mode indicator f_m. R^2 is the traditional coefficient; R^2_{adj} is the adjusted R^2; R^2_{pred} is the prediction R^2.

Resp. Var.	S	R^2	R^2_{adj}	R^2_{pred}
E	1.65667	91.35%	90.79%	90.00%
UTS	9.27990	88.54%	87.80%	87.15%
ε_f	0.000270303	75.71%	74.13%	71.75%

With the associated p-values for all response variables retaining statistical significance, the normalised models support the interpretation that thickness modifies the per-ply efficiency and contribution through greater interlaminar stress redistribution, reduced sensitivity to unbalanced peel stresses, and a greater ability to redistribute damage through more platelets.

Despite the improved performance of the normalised models, particularly for E/n_p and UTS/n_p, the lack-of-fit remains significant. This indicates that first-order normalised models capture the dominant meso-scale architecture–property relationships, but do not fully describe the coupled mechanics of woven EPPs. In particular, interaction effects between l_p, w_p, δl, δw, and n_p are expected since stress-transfer is governed by a three-dimensional network of axial load transfer, transverse redistribution, interlaminar shear, and FPZ development. The normalised predictive models should be interpreted as design-screening tools that quantify the dominant factor effects rather than as complete fracture mechanics models.

4.4. Normalised interpretative models

This section implements models of the kind of Eq. (10). These additional models were introduced following the improved variability description given by f_m in the first order analysis of Section 4.2. In Fig. 17, the effect of f_m is still relevant and linear. However, the introduction of this variable means that the models cannot be utilised in a predictive fashion as in Section 4.3. The three model equations were reported in Eq. (25), (26), and (27), whereas the associated R^2 values were reported in Table 8.

$$\begin{aligned} \frac{E\,[\mathrm{GPa}]}{n_p} &= \beta_{0,f_m} - 0.073n_l - 0.996n_w \\ &\quad +1.098\delta l + 0.251\delta w - 2.3420n_p \\ \beta_{0,FP} &= 29.28 \qquad \beta_{0,FP-TI} = 27.50 \\ \beta_{0,PP} &= 25.51 \qquad \beta_{0,PP-TI} = 26.00 \end{aligned} \tag{25}$$

$$\begin{aligned} \frac{UTS\,[\mathrm{MPa}]}{n_p} &= \beta_{0,f_m} - 4.695n_l + 4.885n_w \\ &\quad +4.366\delta l - 1.727\delta w - 11.632n_p \\ \beta_{0,FP} &= 142.19 \qquad \beta_{0,FP-TI} = 155.52 \\ \beta_{0,PP} &= 157.41 \qquad \beta_{0,PP-TI} = 153.63 \end{aligned} \tag{26}$$

Table 9
ANOVA tables related to the normalised interpretative models for the response variables (Resp. Var.), including the failure mode indicator f_m. *Source* is the origin of the variance; *DF* are the degrees of freedom; *Seq SS* is the sequential sum of squares, quantifying variability associated to factors in their order of appearance; *Contribution* explains the contribution in percentage; *Adj. SS* is the adjusted sum of squares; *Adj. MS* is the adjusted mean of sum of squares; *F-value* is the ratio between explained and error variabilities; *p-value* is the probability associated to the *F-value*.

Resp. Var.	Source	DF	Seq. SS	Contribution	Adj. SS	Adj. MS	F-value	p-value
E	Regression	8	3566.71	91.35%	3566.71	445.84	162.44	0.000
	$n_l\,[\frac{l_o}{l_p}]$	1	21.87	0.56%	0.57	0.57	0.21	0.650
	$n_w\,[\frac{w_o}{w_p}]$	1	222.05	5.69%	118.97	118.97	43.35	0.000
	$\delta l\,[\frac{l_p}{d_l}]$	1	16.07	0.41%	105.29	105.29	38.36	0.000
	$\delta w\,[\frac{w_p}{d_w}]$	1	13.70	0.35%	7.95	7.95	2.90	0.091
	n_p	1	3096.35	79.31%	2704.18	2704.18	985.28	0.000
	f_m	3	196.67	5.03%	196.67	65.56	23.89	0.000
	Error	123	348.57	8.65%	348.57	2.74		
	Lack-of-Fit	43	303.40	7.77%	314.40	7.06	16.51	0.000
	Pure error	80	34.18	0.88%	34.18	0.43		
	Total	131	3904.29	100.00%				
UTS	Regression	8	81 854.4	88.54%	81 854.4	10 231.8	118.81	0.000
	$n_l\,[\frac{l_o}{l_p}]$	1	1936.5	2.09%	2365.8	2365.8	27.47	0.000
	$n_w\,[\frac{w_o}{w_p}]$	1	4865.0	5.26%	2860.9	2860.9	33.22	0.000
	$\delta l\,[\frac{l_p}{d_l}]$	1	6574.2	7.11%	1665.7	1665.7	19.34	0.000
	$\delta w\,[\frac{w_p}{d_w}]$	1	408.7	0.44%	376.7	376.7	4.37	0.039
	n_p	1	64 393.4	69.65%	66 702.1	66 702.1	774.56	0.000
	f_m	3	3676.5	3.99%	3676.5	1225.5	14.23	0.000
	Error	123	10 592.3	11.46%	10 592.3	86.1		
	Lack-of-Fit	43	9838.1	10.64%	9838.1	228.8	24.27	0.000
	Pure error	80	754.3	0.82%	754.3	9.4		
	Total	131	92 446.7	100.00%				
ε_f	Regression	8	0.000028	75.71%	0.000028	0.000004	47.92	0.000
	$n_l\,[\frac{l_o}{l_p}]$	1	0.000000	0.58%	0.000001	0.000001	15.05	0.000
	$n_w\,[\frac{w_o}{w_p}]$	1	0.000007	19.95%	0.000004	0.000004	50.07	0.000
	$\delta l\,[\frac{l_p}{d_l}]$	1	0.000001	2.04%	0.000000	0.000000	6.15	0.061
	$\delta w\,[\frac{w_p}{d_w}]$	1	0.000001	1.50%	0.000000	0.000000	5.07	0.073
	n_p	1	0.000011	29.44%	0.000014	0.000014	192.50	0.000
	f_m	3	0.000008	22.20%	0.000008	0.000003	37.47	0.000
	Error	123	0.000009	24.29%	0.000009	0.000000		
	Lack-of-Fit	43	0.000009	23.00%	0.000009	0.000000	33.38	0.000
	Pure error	80	0.000000	1.29%	0.000000	0.000000		
	Total	131	0.000037	100.00%				

$$
\begin{aligned}
\frac{\varepsilon_f\,[\#]}{n_p} &= \beta_{0,f_m} - 0.0001012 n_l \\
&\quad +0.0001747 n_w - 0.0000717\delta l \\
&\quad -0.0000542\delta w - 0.0001689 n_p \\
\beta_{0,FP} &= 0.002360 \qquad \beta_{0,FP-TI} = 0.002820 \\
\beta_{0,PP} &= 0.003137 \qquad \beta_{0,PP-TI} = 0.003000
\end{aligned}
\tag{27}
$$

The inclusion of the categorical failure morphology improved the descriptive capability of all the normalised models. The R^2_{adj} for E/n_p increased from 85.77% to 90.79%, while UTS/n_p increased from 83.95% to 87.80%. The largest improvement was observed for ε_f/n_p, where R^2_{adj} increased from 51.67% to 74.13%. The categorical intercepts are interpreted as fracture specific offsets, and for the failure responses the PP morphology exhibited the largest intercepts, followed closely by PP$-TI$ and FP$-TI$, while FP exhibits the lowest intercepts. This indicates that the PP morphologies are associated with greater apparent failure resistance and strain capacity. This is consistent with the arresting, deflection, or bridging by neighbouring platelets of a matrix crack propagation, allowing additional energy dissipation prior to failure. Meanwhile, FP morphologies correspond to cases where a resulting dominant crack path propagates through the laminate thickness.

The ANOVA results in Table 9 show that f_m is statistically significant for all the normalised response variables. Furthermore, the inclusion of f_m simply modulated the effect of the DoE factors without reversing the coefficient signs. This indicates that f_m captures additional variability associated with fracture development that the predictive model does not while preserving the factor trends and principal architecture–property relationships.

5. Conclusions

This work investigated the viability of aligned woven discontinuous platelets, focusing on characterising the tensile properties of various woven engineered prepreg platelet (EPP) architectures and identifies the key platelet parameters that most significantly affect composite performance. The thorough experimental campaign tested 132 EPP specimens following the ASTM D3039 standard [35]. The measured tensile properties were then statistically analysed adopting *ANOVA* to identify the effects of the DoE factors.

The first key outcome was that simple first-order linear models were insufficient to properly describe the woven EPP mechanics. The introduction of the failure mode factor (f_m) significantly improved the responses' capability of describing variability to approximately 60% – 66%, highlighting that the elastic response for engineered platelet-based composites is not purely driven by the platelet's manufacturing parameters. Rather it is strongly coupled to the damage and propagation state, confirming that the tensile E, UTS, and ε_f are entangled through stress redistribution and fracture evolution for woven EPP composite systems.

Most importantly, normalising responses by ply count (E/n_p, UTS/n_p, or ε_f/n_p) resulted in a strong linearisation of trends, allowing for the predictive use of the models. The normalised first-order models reach a high capability of describing the variability for stiffness and strength ($R^2_{adj} \approx$ 84–86%), confirming that a large portion of the perceived nonlinearity originates from thickness scaling effects alongside the role of n_p in the load-transfer network and shear-lag efficiency. The normalised ε_f/n_p improved as well, but remained notably weaker at $R^2_{adj} \approx$ 52%, consistent wit the failure strain being more sensitive to progressive damage and the existence of a textile pattern cut a differing portions influencing the model's ability to interpret variability.

From the ANOVA, the following design-relevant effects were identified:

- Ply count n_p dominates the variance of absolute properties, remaining statistically significant in the normalised models. This highlights that thickness does not merely scale an architecture's response, but alters per-ply efficiency.
- Increasing n_l reduces the per-ply stiffness and strength, as the smaller platelets increase the longitudinal discontinuity density, resulting in more matrix-dominated inter-ply segments along the axial load-path increasing the most common failure initiation sites.
- Increasing n_w reduces per-ply stiffness, but increases strength and ductility metrics, indicating a shift towards more distributed damage and energy dissipation at the cost of rigidity.
- δl shows a positive influence, favouring larger longitudinal superpositions, underlining the criticality of overlap continuity along the primary load-transfer direction.
- δw has the least influence, suggesting that within the tested bounds, transverse overlap is secondary to the remaining DoE factors in the investigated study.

Overall, *ANOVA* results establish that woven EPP tensile performance is governed by:

- Thickness-driven scaling.
- Discontinuity controlled load transfer.

Per-ply normalised linear models provide a practical and interpretable basis for design screening of EPP architectures. Furthermore, they highlight which parameters affect the performance, producing tailorable platelet-based engineered composites which can modify the in-ply properties of the material without modification to the manufacturing process or base material system. Meanwhile, explicit failure-mode coupling and higher-order effects are required to robustly predict ductility and fracture behaviour across the full design space.

Future work should incorporate full-field strain measurement techniques, such as Digital Image Correlation (DIC), to resolve the local deformation mechanisms that cannot be captured using conventional extensometers [42]. For woven EPPs, DIC would enable the axial and shear strain fields around platelet edges to be visualised directly. This would provide clearer experimental evidence of local strain amplification, shear-lag stress transfer, the formation of localised bands prior to macroscopic failure. It would also help clarify the role of the transverse reinforcement with regards to redistributing or arresting local damage.

Furthermore, DIC-derived measurements, such as strain-concentration factors, maximum local strain, and the localisation onset strain could be used as physical-based descriptors for future analytical or numerical damage predicting models, allowing for a more defined architecture–property relationship using shear-lag theory as a foundation.

Nomenclature

ANOVA	Analysis of Variance
BaM	Brick-and-Mortar
CFRP	Carbon fibre reinforced polymer
DoE	Design of Experiments
DCFC	Discontinuous fibre composites
DIC	Digital Image Correlation
E	Young's Modulus
EPP	Engineered prepreg platelets
f_m	Failure mode factor
FP	Full propagation
FP-TI	Full propagation with by tab-influence
FPZ	Fracture Process Zone
n_l	Number of platelets in specimen length
n_p	Number of plies
n_w	Number of platelets in specimen width
l_p	Platelet length
α	Platelet length-to-thickness aspect ratio
ω	Platelet width-to-thickness aspect ratio
δl	Platelet length superposition
w_p	Platelet width
δw	Platelet width superposition
PPMC	Prepreg platelet moulded composite
PP	Partial propagation
PP-TI	Partial propagation with by tab-influence
RVE	Representative Volume Element
L_C	Platelet Critical Length
SEM	Scanning Electron Microscopy
s_E	Standard deviation of E
s_{ε_f}	Standard deviation of strain at failure
s_{UTS}	Standard deviation of UTS
l_0	Specimen length or gauge length
w_0	Specimen width
ε_f	Strain at failure
TBDC	Tow based discontinuous composites
UD	Unidirectional
UTM	Universal testing machine
UTS	Ultimate tensile strength

CRediT authorship contribution statement

Alessandro Masetti Placci: Writing – review & editing, Writing – original draft, Visualization, Validation, Project administration, Methodology, Investigation, Formal analysis, Data curation, Conceptualization. **Luca Bernini:** Writing – review & editing, Writing – original draft, Visualization, Validation, Supervision, Methodology, Conceptualization. **Paolo Albertelli:** Validation, Supervision, Methodology, Conceptualization.

Declaration of competing interest

The authors declare the following financial interests/personal relationships which may be considered as potential competing interests: Alessandro Masetti Placci reports financial support was provided by Racing Bulls S.p.A. Alessandro Masetti Placci reports a relationship with Racing Bulls S.p.A. that includes: consulting or advisory. No additional known competing financial interests or personal relationships exist which could have appeared to influence the work reported in this paper.

Acknowledgements

Project funded under the National Recovery and Resilience Plan (NRRP), Mission 04 Component 2 Investment 1.5—NextGenerationEU, Call for tender n. 3277 dated 30 December 2021 Award Number: 0001052 dated 23 June 2022. The authors would like to thank Racing Bulls S.p.A. Formula One Team for funding the manufacturing of specimens and providing their industrial knowledge and experience for the production of composites.

Data availability

Data will be made available on request.

References

[1] Harris CE, Starnes JH, Shuart MJ. Design and manufacturing of aerospace composite structures, state-of-the-art assessment. J Aircr 2002;39(4):545–60. http://dx.doi.org/10.2514/2.2992.

[2] Masetti Placci A, Bernini L, Albertelli P, Cimino C, Perotti F, Monno M. A review on circular economy approaches for pre-impregnated carbon composites mould remanufacturing. Int J Precis Eng Manuf.-Green Technol 2025. http://dx.doi.org/10.1007/s40684-025-00776-3.

[3] Montagna LS, Morgado GFd, Lemes AP, Passador FR, Rezende MC. Recycling of carbon fiber-reinforced thermoplastic and thermoset composites: A review. J Thermoplast Compos Mater 2022;36:3455–80. http://dx.doi.org/10.1177/08927057221108912.

[4] Campbell FC. Structural composite materials. ASM International; 2010, p. 612. http://dx.doi.org/10.1007/978-981-99-5982-2.

[5] Intelligence M. Carbon fiber reinforced plastic (CFRP) market size and share source. 2026, URL: https://www.mordorintelligence.com/industry-reports/carbon-fiber-reinforced-plastic-market. Report.

[6] Nakagawa T, Ko S, Houser G, Yang J, Salviato M. Repurposed discontinuous fiber composites for industrial applications: Effects of average number of platelets through the thickness, platelet length, and hybridization on flexure properties. Compos A 2024;180:108046. http://dx.doi.org/10.1016/j.compositesa.2024.108046.

[7] Sloan J. The outlook for carbon fiber supply and demand. 2025, URL: https://www.compositesworld.com/articles/the-outlook-for-carbon-fiber-supply-and-demand.

[8] Zhang J, Chevali VS, Wang H, Wang C-H. Current status of carbon fibre and carbon fibre composites recycling. Compos B 2020;193:1–15. http://dx.doi.org/10.1016/j.compositesb.2020.108053.

[9] Nilakantan G, Nutt S. Reuse and upcycling of thermoset prepreg scrap: Case study with out-of-autoclave carbon fiber/epoxy prepreg. J Compos Mater 2017;52(3):341–60. http://dx.doi.org/10.1177/0021998317707253.

[10] Schwarz S, Höftberger T, Burgstaller C, Hackl A, Schwarzinger C. Pyrolytic recycling of carbon fibers from prepregs and their use in polyamide composites. Open J Compos Mater 2020;10(04):92–105. http://dx.doi.org/10.4236/ojcm.2020.104007.

[11] Kumar S, Krishnan S. Recycling of carbon fiber with epoxy composites by chemical recycling for future perspective: a review. Chem Pap 2020;74(11):3785–807. http://dx.doi.org/10.1007/s11696-020-01198-y.

[12] Pimenta S, Pinho ST. Recycling carbon fibre reinforced polymers for structural applications: Technology review and market outlook. Waste Manage 2011;31(2):378–92. http://dx.doi.org/10.1016/j.wasman.2010.09.019.

[13] Wan Y, Takahashi J. Tensile properties and aspect ratio simulation of transversely isotropic discontinuous carbon fiber reinforced thermoplastics. Compos Sci Technol 2016;137:167–76. http://dx.doi.org/10.1016/j.compscitech.2016.10.024.

[14] Kravchenko SG, Sommer DE, Pipes RB. Uniaxial strength of a composite array of overlaid and aligned prepreg platelets. Compos A 2018;109:31–47. http://dx.doi.org/10.1016/j.compositesa.2018.02.032.

[15] Sommer DE, Kravchenko SG, Pipes RB. Investigation of the notch sensitivity of tailorable long fiber discontinuous prepreg composite laminates. Compos A 2025;188:108508. http://dx.doi.org/10.1016/j.compositesa.2024.108508.

[16] Aranke SS, Pipes RB. Platelet critical length for prepreg platelet molded composites. Compos A 2024;181:108142. http://dx.doi.org/10.1016/j.compositesa.2024.108142.

[17] Alves M, Pimenta S. The influence of 3D microstructural features on the elastic behaviour of tow-based discontinuous composites. Compos Struct 2020;251:112484. http://dx.doi.org/10.1016/j.compstruct.2020.112484.

[18] Ryatt J, Ramulu M. Prediction of tensile failure of stochastic tow-based discontinuous composites via mesoscale finite element analysis. Compos Struct 2022;279:114769. http://dx.doi.org/10.1016/j.compstruct.2021.114769.

[19] Wan Y, Takahashi J. Tensile and compressive properties of chopped carbon fiber tapes reinforced thermoplastics with different fiber lengths and molding pressures. Compos A 2016;87:271–81. http://dx.doi.org/10.1016/j.compositesa.2016.05.005.

[20] Feraboli P, Peitso E, Deleo F, Cleveland T, Stickler PB. Characterization of prepreg-based discontinuous carbon fiber/epoxy systems. J Reinf Plast Compos 2008;28(10):1191–214. http://dx.doi.org/10.1177/0731684408088883.

[21] Wyser Y, Leterrier Y, Månson J-AE. Analysis of failure mechanisms in platelet-reinforced composites. J Mater Sci 2001;36(7):1641–51. http://dx.doi.org/10.1023/a:1017583432728.

[22] Yamashita S, Hashimoto K, Suganuma H, Takahashi J. Experimental characterization of the tensile failure mode of ultra-thin chopped carbon fiber tape-reinforced thermoplastics. J Reinf Plast Compos 2016;35(18):1342–52. http://dx.doi.org/10.1177/0731684416651134.

[23] Ko S, Yang J, Tuttle ME, Salviato M. Effect of the platelet size on the fracturing behavior and size effect of discontinuous fiber composite structures. Compos Struct 2019;227:1–13. http://dx.doi.org/10.1016/j.compstruct.2019.111245.

[24] Nakagawa T, Ko S, Houser G, Yang J, Salviato M. Flexural performance of hybrid discontinuous fiber composites made of repurposed aerospace prepreg. In: American society for composites 2022. ASC37, Destech Publications, Inc.; 2022, p. 1–13. http://dx.doi.org/10.12783/asc37/36435.

[25] Kravchenko SG, Sommer DE, Denos BR, Avery WB, Pipes RB. Structure-property relationship for a prepreg platelet molded composite with engineered meso-morphology. Compos Struct 2019;210:430–45. http://dx.doi.org/10.1016/j.compstruct.2018.11.058.

[26] Lakes R. Materials with structural hierarchy. Nature 1993;361(6412):511–5. http://dx.doi.org/10.1038/361511a0.

[27] Aitharaju V, Averill R. Three-dimensional properties of woven-fabric composites. Compos Sci Technol 1999;59(12):1901–11. http://dx.doi.org/10.1016/s0266-3538(99)00049-4.

[28] Chowdhury IR, Summerscales J. Woven fabrics for composite reinforcement: A review. J Compos Sci 2024;8(7):280. http://dx.doi.org/10.3390/jcs8070280.

[29] Ashby MF. The design process. In: Materials selection in mechanical design. Elsevier; 2011, p. 15–29. http://dx.doi.org/10.1016/b978-1-85617-663-7.00002-3, [Chapter 2].

[30] Visa Cashapp R. Visa Cashapp RB racing bulls F1 team. 2024, URL: https://www.visacashapprb.com/en/.

[31] Ko S, Nakagawa T, Chen Z, Avery WB, Adams EJ, Soja MR, Larson MH, Park CY, Yang J, Salviato M. Effects of average number of platelets through the thickness and platelet width on the mechanical properties of discontinuous fiber composites. Compos A 2024;177:107945. http://dx.doi.org/10.1016/j.compositesa.2023.107945.

[32] Srl B. Componenti in materiali compositi avanzati. 2024, URL: https://www.blacks-composites.it/.

[33] CIT. CIT composite materials Italy. 2024, URL: https://www.composite-materials.it/pagina.php.

[34] Lectra. Lectra automotive. 2025, URL: https://www.lectra.com/en/automotive#form.

[35] ASTM. D3039/D3039M standard test method for tensile properties of polymer matrix composite materials. 2024, http://dx.doi.org/10.1520/D3039_D3039M-17.

[36] Cox HL. The elasticity and strength of paper and other fibrous materials. Br J Appl Phys 1952;3(3):72–9. http://dx.doi.org/10.1088/0508-3443/3/3/302.

[37] Pipes RB, Pagano N. Interlaminar stresses in composite laminates under uniform axial extension. J Compos Mater 1970;4(4):538–48. http://dx.doi.org/10.1177/002199837000400409.

[38] Daniel IM, Ishai O. Engineering mechanics of composite materials. USA: Oxford University Press; 1994.

[39] Fazlali B, Lomov SV, Swolfs Y. Reducing stress concentrations in static and fatigue tensile tests on unidirectional composite materials: A review. Compos B 2024;273:111215. http://dx.doi.org/10.1016/j.compositesb.2024.111215.

[40] Montgomery D. Design and analysis of experiments. 5th ed.. John Wiley and Sons; 2001.

[41] Aranke SS. Interlaminar fracture in prepreg platelet molded composites [Ph.D. thesis], Purdue University; 2024, http://dx.doi.org/10.25394/PGS.27089629.v1, URL: https://hammer.purdue.edu/articles/thesis/Interlaminar_Fracture_in_Prepreg_Platelet_Molded_Composites/27089629.

[42] Chen S, Zhang R, Shi Z, Lin J. An improved DIC method for full-field strain measurement in tensile tests on aluminium alloys under hot stamping conditions. Int J Light Mater Manuf 2024;7(3):438–49. http://dx.doi.org/10.1016/j.ijlmm.2024.01.001.